THE ASTROPHYSICAL JOURNAL, 343:177–200, 1989 August 1


# H I ABSORPTION MEASUREMENTS OVER THE GALACTIC CENTER RADIO ARC REGION

J. LASENBY AND A. N. LASENBY
Mullard Radio Astronomy Observatory, Cambridge
AND
F. YUSEF-ZADEH[1]
Laboratory for Astronomy and Solar Physics, NASA-Goddard Space Flight Center; and Northwestern University
*Received 1988 August 23; accepted 1989 January 18*

## ABSTRACT

An H I absorption study of the central ~100 pc of the Galactic center was performed using the compact array of the Very Large Array (VLA).[2] The observations revealed an apparent absence of gas at 40–50 km $s^{-1}$ across the filamentary structure known as the Radio Arc. There is strong evidence that the body of gas at 40–50 km $s^{-1}$, known as the "40 km $s^{-1}$ molecular cloud," is intimately related to the nucleus, Sgr A, but the lack of absorption across the Arc indicates that the cloud is placed behind the Arc—a conclusion at variance with other observations which suggest a close relationship between the 40 km $s^{-1}$ material and the Radio Arc. In addition, gas around +20 km $s^{-1}$ was observed to cover the length of the Radio Arc filaments except for a gap around the central region where the Arc crosses the Galactic plane. The gap coincides exactly with a lobe of 3 cm polarized emission. This leads us to suppose that the radio emission from the Arc filaments is synchrotron in origin but that much of the emission is depolarized by the 20 km $s^{-1}$ gas. The distribution of H I gas at negative velocities (−10 to −60 km $s^{-1}$) across a series of curved structures apparently connecting the Arc to the Sgr A complex (known as the arched filaments or the "Arches") confirms the kinematic structure revealed by high-resolution molecular and radio recombination line observations and strongly suggests an association of the negative velocity H I gas with the ionized filaments. Comparisons of various H I and molecular peaks lead to possible positionings of the material relative to the continuum. The optical depth maps, formed via a new statistical technique and at a resolution of ~40″ (chosen so as to concentrate on the larger scale structures of the Radio Arc and Arches), also clearly show the ~3 pc rotating ring of gas and dust about Sgr A* as well as a number of interesting features in the vicinity of Sgr A; a detailed discussion of Sgr A and its immediate environment will appear in a later paper (Lasenby *et al.* 1989).

*Subject headings:* galaxies: internal motion — galaxies: nuclei — galaxies: The Galaxy — radio sources: 21 cm radiation

## I. INTRODUCTION

The Galactic center is now known to be a region exhibiting strange radio structure and unusual mixtures of thermal and nonthermal emission, as shown recently by Yusef-Zadeh, Morris, and Chance 1984. The Radio Arc consists of a system of narrow filamentary structures aligned almost perpendicular to the Galactic plane at $l \simeq 0\overset{\circ}{.}18$, while a series of curved structures, the Arches, appear to connect the Arc to the Sgr A halo. There is also evidence of faint helical features apparently winding around the filaments of the Arc. Such exotic structure may well point to a large-scale structured magnetic field controlling the gas dynamics (Yusef-Zadeh *et al.* 1984). Any attempt to explain such a field by processes occurring within Sgr A will, of course, require firm establishment that the Radio Arc indeed lies at the Galactic center and is not a chance superposition of a foreground object. Throughout this paper we shall take the distance to the galactic center ($D_{gc}$) to be 8.5 kpc, and all distance estimates will therefore be based on this value.

The large molecular clouds in the Galactic center region are concentrated mostly within $R \sim 250$ pc, where $R$ is the radial distance from the galactic nucleus (Bania 1977), with the strongest molecular emission being found mainly at positive velocities and positive longitudes (see, for example, Bally *et al.* 1987). Two main concentrations dominate this region; one occurs at longitude ~0° and is known as the Sgr A complex. The Sgr A molecular complex has its emission centered on ~+40 km $s^{-1}$ and is often referred to as the 40 km $s^{-1}$ molecular cloud. While it is now generally accepted that this cloud lies very close to the Galactic nucleus, there is still controversy as to its precise situation with respect to the Sgr A radio sources and the Radio Arc (see Brown and Liszt 1984 for a useful discussion of the various arguments).

Yusef-Zadeh *et al.* 1984, have outlined several arguments supporting the claim that the filaments of the Radio Arc are related to the Galactic nucleus, and one of the most convincing of these involves the appearance of the 40 km $s^{-1}$ cloud in $NH_3$(1, 1) emission. $NH_3$(1, 1) emission contours at 40 km $s^{-1}$ (Güsten, Walmsley, and Pauls 1981) appear to trace the outline of G0.18−0.04, a radio structure often called the "sickle" due to its shape, seen where the filaments cross the Galactic plane. Further evidence is provided by the recombination line emission from the sickle observed by Pauls and Mezger (1980). Here it was found that the sickle feature was the only region to display significant emission around +40 km $s^{-1}$. The high-resolution 6 cm mapping of the Radio Arc by Yusef-Zadeh (1986, hereafter YZ86), has shown that there is a good case for sickle-filament interaction. For instance, some filaments appear brighter on the negative latitude side of the sickle than

[1] National Research Council Resident Research Associate.

[2] The VLA is part of the National Radio Astronomy Observatory which is operated by Associated Universities, Inc., under contract with the US National Science Foundation.

on the positive latitude side, indicating possible energy dissipation on crossing the sickle. Also, in several filaments there are slight signs of structural discontinuities as they pass through the sickle. Thus, if the sickle can be shown to be interacting with the 40 km $s^{-1}$ cloud, it would follow that we could place the Radio Arc at the Galactic center.

In an attempt to further establish this possible connection between the Arc and the 40 km $s^{-1}$ cloud, we carried out an H I absorption study of the Sgr A–sickle-Arc region using the C/D array of the VLA. Absorption of the radio continuum from the sickle and Arc by the 40 km $s^{-1}$ cloud would place the filaments *behind* this cloud and thus strongly support their positioning at the Galactic center. No apparent absorption would imply either that the filaments were in *front* of the cloud or that the column density of the 40 km $s^{-1}$ cloud drops off abruptly where the filaments begin. In addition, the study was aimed at giving more general information, over the whole field of view, on the relative positionings of the molecular condensations with respect to the radio continuum features, and on whether the molecular distribution could be closely tied to the continuum structure. There have recently been several ideas as to the origin of the Arc; for example, it has been postulated that the Arc may be caused by the shocks generated when orbiting molecular gas collides with almost stationary gas in the Galactic plane (Bally *et al.* 1988). The H I absorption study on the scale described here may provide a means of testing some of these postulates.

The previous absence of H I absorption observations over a relatively large field of view comprising the inner $\sim 80$ pc of the Galaxy, is particularly conspicuous given the current interest in the origin and structure of the bizarre radio emission close to the Galactic nucleus. Past H I absorption synthesis studies had been confined to high-resolution work on Sgr A (e.g., Schwarz, Shaver, and Ekers 1977; Liszt *et al.* 1983; Radhakrishnan and Sarma 1980). The present lower resolution synthesis study over a wide velocity range was designed not only to be complementary to such high-resolution observations, having sensitivity to lower brightness, larger scale structure rather than point sources, but also to relate to angular scales similar to many CO studies.

## II. OBSERVATIONS

The H I absorption observations of the Galactic center region to be described here were carried out using the VLA C/D hybrid array in 1985 November. The use of the hybrid array with a long north arm allows for the foreshortening of the north-south baseline components when observing a low declination source and therefore produces an approximately circular beam. Spectral line observations were made at the 21 cm hydrogen line frequency ($\nu \simeq 1.42$ GHz) in Mode 2A with online Hanning smoothing. Sixty-four channels separated by $\sim 48.828$ kHz were used, giving a total bandwidth of 3.125 MHz. The velocity resolution was thus $\sim 10.2$ km $s^{-1}$ and the total velocity coverage $\sim 660$ km $s^{-1}$. The velocity range of approximately $\pm 300$ km $s^{-1}$ was expected to include most of the interesting features. The use of 64 channels restricted the number of antennas to 18, and these were chosen so as to achieve optimal *u-v* coverage consistent with an intermediate resolution and sensitivity to weaker, extended structure. The maximum and minimum baselines were then $\sim 1$ km and 45 m, respectively. The field of view in the C/D configuration at 20 cm was $\sim 40'$, centered on G0.18 − 0.04 at $\alpha = 17^h43^m32^s$, $\delta = 28°47'3''.0$, so that the field included the region out to the Sgr B2 complex ($\sim 100$ pc from the Galactic nucleus).

The observing run lasted for some 8 hr during which time 3C 286 ($S_{1.42} = 14.73$ Jy), 3C 48 ($S_{1.42} = 15.76$ Jy) and Cygnus A were observed as flux calibrators, and 1748−253 as a phase calibrator. To avoid any possible H I absorption, the rest frequency was offset from 1420.406 MHz to 1419.006 MHz while observing the calibrators. The $T_{sys}$ correction for line observations was applied online.

Calibration of the data was carried out on the DEC 10 at the VLA using standard routines, and Cygnus A was chosen as being the best source for use as a bandpass calibrator to eliminate the instrumental response. The PIPELINE facility at the VLA was used to make the channel maps; this takes calibrated *u-v* data, produces maps and will perform operations such as addition, subtraction, CLEAN (Clark 1980), and so on. Two sets of 256 × 256 line maps were made for channels 5–55 (corresponding to velocities of $\sim 280$ to $-240$ km $s^{-1}$) using *uniform* and *natural* weightings. A cell size of 18″ was used which, since the C/D array at 20 cm has a synthesized beamwidth of $\sim 50''$, gave $\sim 2.8$ points per beam. Two continuum maps (C1 and C2) were made by separately averaging channels 9–13 (C1) and 49–53 (C2), these ranges being chosen since they were free from both absorption and end effects. Using C1 for channels 5–32 and C2 for channels 33–55, difference (line minus continuum) maps were made; the use of two separate continuum maps in this way minimized any effects from the change in beamshape with frequency across the band. Figures 1*a* and 1*b* show gray-scale and contour representations of the continuum map made by averaging C1 and C2. The standard CLEAN package on the VLA pipeline was used to deconvolve the dirty beam from the inner quarter of each dirty map; again to minimize the effects of a possibly varying beam shape, a series of beams taken from across the band were used in this process. We chose to clean the resultant difference map in preference to cleaning the individual line and continuum maps separately and then subtracting in the clean-map domain. Since CLEAN is a nonlinear process, subtracting the CLEANed continuum map from the CLEANed line map will not produce the true line-minus-continuum distribution deconvolved from the instrumental response unless very special precautions are taken. The beams used in the CLEANing process were $\sim 53'' \times 40''$ for uniform weighting and $\sim 72'' \times 60''$ for natural weighting.

The uniformly weighted difference maps for channels 5–55 are shown in Figure 1*c*. The numbers in the top left-hand corner of each map show the central velocity of the channel. It should be noted here that the maps of Figure 1 have *not* been corrected for primary beam attenuation. As the extent of the structure in which we are interested is $\sim 30'$, and the primary beam diameter of the VLA at 20 cm is $\sim 35'$, the fluxes near the edges of the maps will be down by $\sim 50\%$ from their true values. This will not, however, affect the calculation of quantities, such as optical depth, formed from the division of two maps; this point is discussed more fully in the following section.

## III. ANALYSIS

In the difference maps, the intensity distribution depends on both the background continuum and on the foreground absorbing gas. It is consequently desirable also to have maps of H I optical depth, $\tau$(H I). Since $\tau$ is a measure of the *absorption*

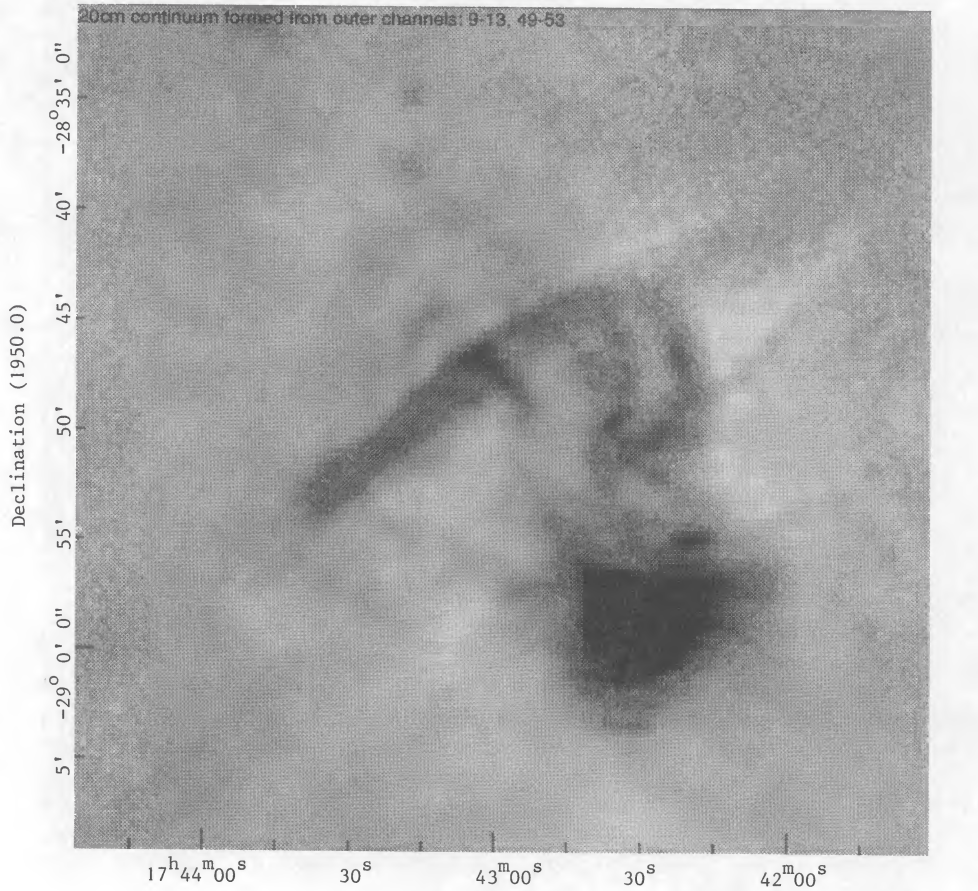


FIG. 1*a*

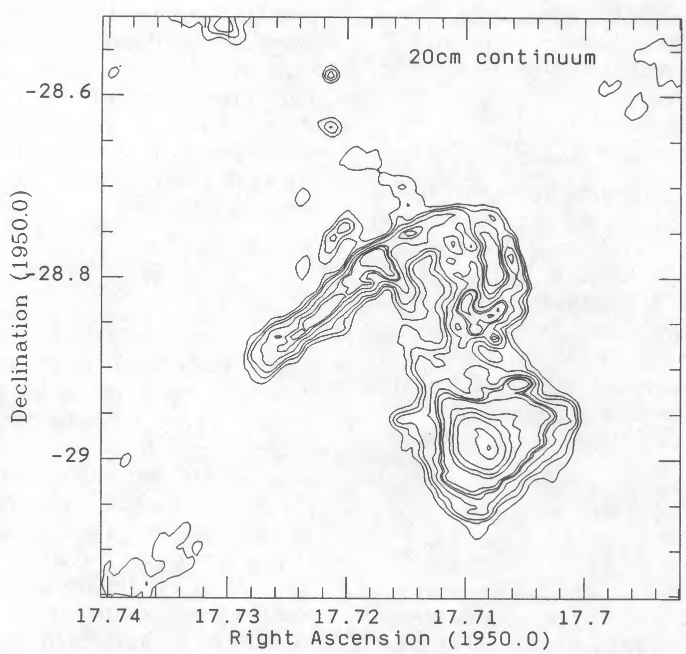


FIG. 1*b*

FIG. 1.—(*a*) 20 cm continuum map made by averaging the outer channels (9–13 and 49–53), shown on a scale ranging from 0(white) to 0.5(black) in units of log (Jy per beam). (*b*) The 20 cm continuum map of (*a*) shown in contour form. Levels are 0.1, 0.2, 0.3, 0.4, 0.5, 0.7, 0.8, 1.0, 2.0, 3.0, 5.0, 10.0, and 14.0 Jy beam$^{-1}$. (*c*) H I absorption line-minus-continuum (difference) maps for channels 5–55. The central velocity of the channel is shown in the top left-hand corner of each frame. In every channel map the negative log of the absolute value of the difference (in Jy per beam) has been taken, and the gray-scale range is 0(white) to $-0.5$(black) in all cases. Each frame covers the same area as shown in (*a*) and (*b*). The maps have *not* been corrected for primary beam attenuation.

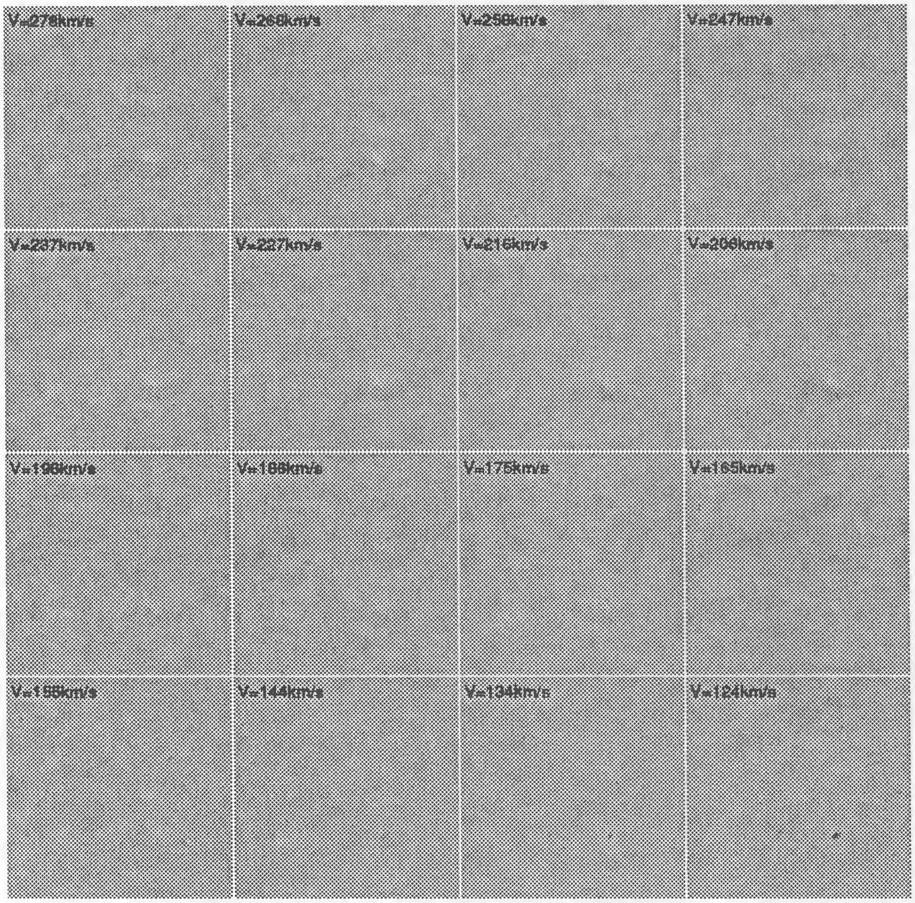


FIG. 1*c*—*Continued*

and hence of the column density of the foreground gas, it is *not* dependent on the intensity of the background continuum.

The optical depth $\tau(\mathrm{H\ I})$ at any point can be written as

$$\tau(\mathrm{H\ I}) = -\ln\left[1 + \frac{I_l - I_c}{I_c - \Omega_b B_\nu(T_{\mathrm{spin}})}\right], \quad (1)$$

where $I_l$ and $I_c$ are the line and continuum intensities in flux per beam, $\Omega_b$ is the beam area, and $T_{\mathrm{spin}}$ is the excitation or spin temperature for the 21 cm spin-flip transition of atomic hydrogen. Note here that $I_l$ denotes the intensity in the channel maps, and thus the expression $I_l - I_c$ is equivalent to the "line intensity" used by some authors. In general, we have little idea of how $T_{\mathrm{spin}}$ varies across the map and it is the usual practice to form maps of $\tau$ using $T_{\mathrm{spin}} = 0$ everywhere. We shall follow this practice here but later attempt to estimate what effect this assumption has on the resultant maps. With $T_{\mathrm{spin}} = 0$, $\tau(\mathrm{H\ I})$ is given by the simple relation

$$\tau(\mathrm{H\ I}) \simeq -\ln\left(1 + \frac{I_l - I_c}{I_c}\right). \quad (2)$$

Taking $T_{\mathrm{spin}} = 0$, it is worth noting that by $I_c$ we are referring to the intrinsic source continuum emission plus the contribution from the cosmic background radiation at the given frequency.

### *a*) *Error Analysis*

In forming $\tau$ from equation (2), we must ask what the errors are in $\tau$ given known errors in $(I_l - I_c)$ and $I_c$. In the study described here we are interested in regions where the absorption is strong and the continuum relatively weak, making this question of particular importance. If $|I_c|$ and $|I_l - I_c|$ become close in value, large errors in $\tau$ become possible, these being most pronounced when both values are not much larger than the noise. In fact, even across the Sgr A region, where the radio continuum is much greater than the rms noise, the possible errors in $\tau$ can be large when the absorption is strong. In the past, the formula

$$\frac{\sigma_\tau}{\tau} \simeq \frac{z}{(1+z)\ln(1+z)}\left[\frac{\sigma_{l-c}{}^2}{(I_l - I_c)^2} + \frac{\sigma_c{}^2}{I_c{}^2}\right]^{1/2}, \quad (3)$$

where $z = (I_l - I_c)/I_c$ and $\sigma_i{}^2$ denotes variance, has been widely used to estimate errors in $\tau$. However, since equation (3) is obtained by assuming all changes are small, it will no longer be valid as $z \to -1$, since then small changes in $z$ can result in large changes in $\tau = -\ln(1+z)$. Past absorption studies have attempted to deal with this problem by imposing cutoffs, i.e., in the production of $\tau$ maps one restricts consideration to those points where the continuum (and possibly also $|\text{line} - \text{continuum}|$) is above a certain value, this value being dictated by the rms noise on the maps. Use of this method makes the resultant errors in $\tau$ rather difficult to quantify, and in many cases the error in $\tau$ is quoted for the point at which the peak continuum flux occurs and nowhere else (see, for example Liszt *et al.* 1983).

To make any meaningful statements about the errors in $\tau$, it is apparent that one needs to investigate the distribution of $\tau$ given the distributions of $I_l - I_c$ and $I_c$, and that simplistic arguments are inadequate. Consequently a statistical tech-

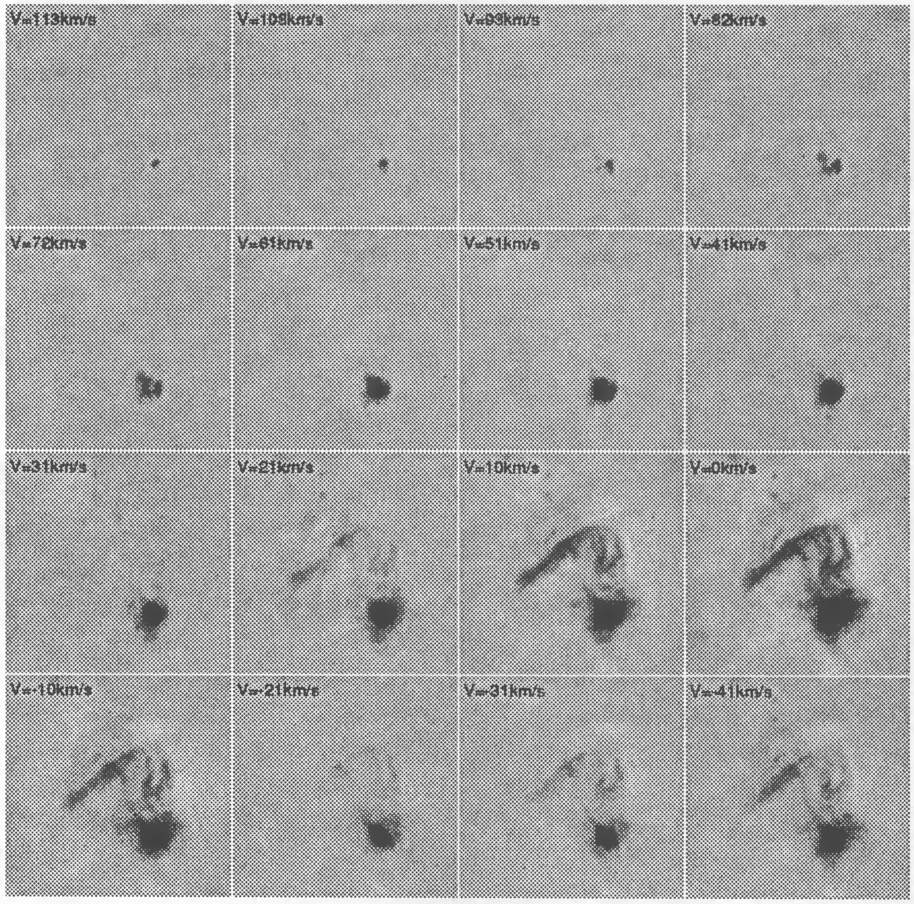


FIG. 1c—*Continued*

nique was derived for producing optical depth maps and is set out in detail in the Appendix. This technique uses a Bayesian analysis to obtain the distribution of $\tau$ given the observations, which can then be used to find a confidence interval for $\tau$. The outcome of this is a criterion for accepting or rejecting the calculated value of $\tau$, which is such that *for all those points at which $\tau_{\rm obs}$ is retained, one can be $\sim$95% confident that the fractional error in $\tau_{\rm obs}$ is $\leq$20%.*

From the discussion in the Appendix it is apparent that by imposing cutoffs, rather than going through an analysis of the type we suggest, one is likely to (*a*) include values of $\tau$ which have a greater than 20% fractional error and (*b*) omit values of $\tau$ which might have a smaller than 20% fractional error.

The result of applying the new statistical analysis is very striking as Figures 2 and 3 illustrate. Figure 2 shows three optical depth maps for channel 13, i.e., $\sim +196$ km s$^{-1}$. Figure 2*a* was made using a cutoff of 0.05 Jy beam$^{-1}$ in $I_c$, Figure 2*b* used cutoffs of 0.1 Jy beam$^{-1}$ in *both* $I_c$ and $|I_l - I_c|$, and Figure 2*c* used the statistical technique outlined above. In Figure 2*a* we see a large amount of spurious structure, while in Figure 2*b*, with stricter cutoffs, much of this disappears. In Figure 2*c* however, there is only one small region in which we can be $\sim$95% confident that the errors in $\tau$ are less than 20%, and a check on this region shows that it coincides with the compact radio source Sgr A*. It is interesting to note that, down to the contour levels displayed, Figures 2*a* and 2*b* show *no* features against Sgr A*! Figure 3 shows the same behavior in one of the high negative velocity channels, i.e., $-186$ km s$^{-1}$. Figure 3*a* was made using a cutoff of 0.10 Jy beam$^{-1}$ in both $|I_l - I_c|$ and $|I_c|$, while Figure 3*b* used the statistical technique. Overall, the statistical method produces much "cleaner" maps on which the errors are quantifiable. In addition to dealing with errors correctly in the case of strong absorption, the method is also effective in eliminating the spurious structure where the absorption is low, i.e., in the outer channels. All $\tau$ maps shown in the rest of this paper have been produced using the statistical technique.

The error analysis described above and in the Appendix was applied to the difference and continuum maps with *no* correction for primary beam attenuation. It can, however, easily be shown that, since the analysis depends solely on signal to noise ratios rather than on individual flux values, we are justified in the use of the uncorrected maps.

### *b) Effects of Nonzero $T_{\rm spin}$*

It was noted previously that the true value of optical depth would depend on how the spin temperature, $T_{\rm spin}$, varied over the map. To investigate the effects of a nonzero $T_{\rm spin}$, several maps were made taking $T_{\rm spin}$ constant across the whole field. Although such a constant value is probably as unrepresentative as a zero value, it will at least illustrate the behavior of $\tau$ when $T_{\rm spin}$ is altered. Figure 4 shows $\tau$ maps for $v = 20$ km s$^{-1}$ made with $T_{\rm spin}$ values of 50 and 100 K. We see that there is little qualitative change in the structure of the maps, but that as $T_{\rm spin}$ increases, so the value of $\tau$ at a given point also increases. There is also a slight increase in the *number* of points rejected

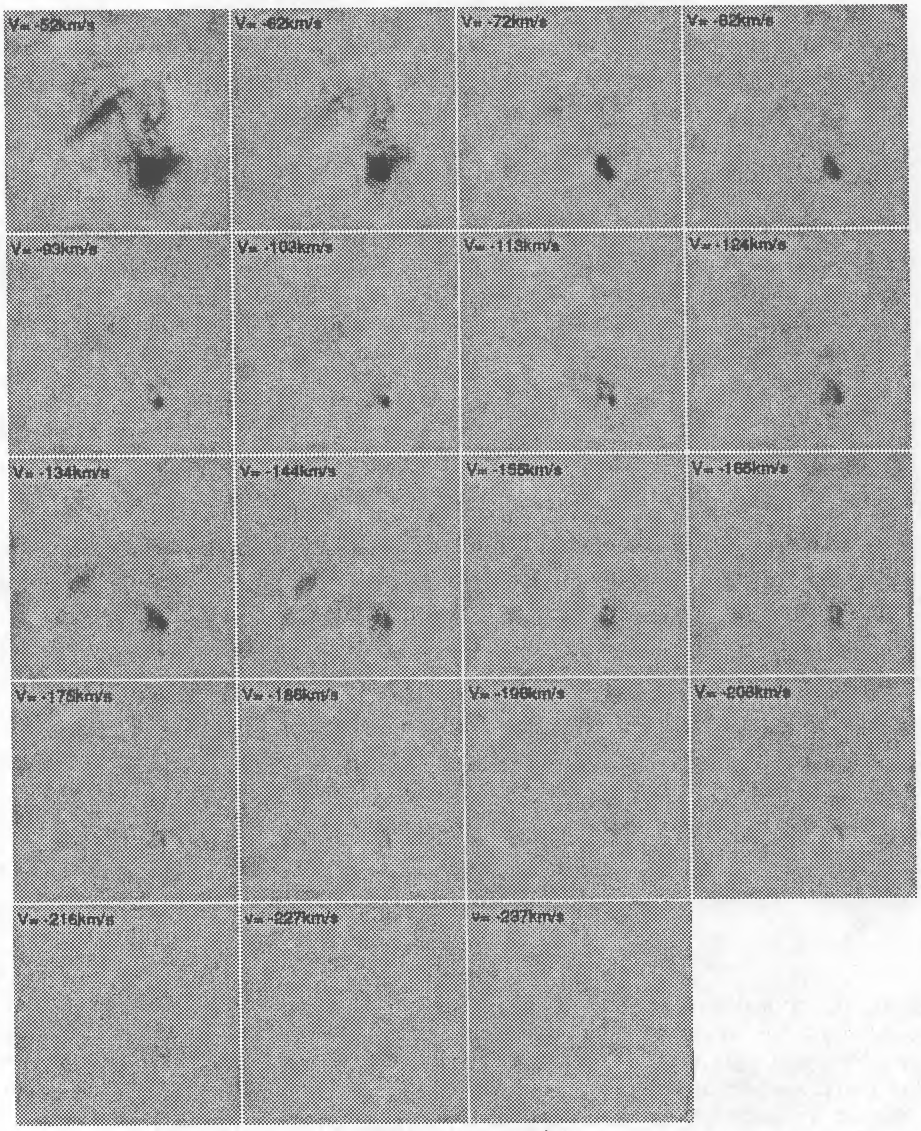


FIG. 1*c*—*Continued*

as $T_{\rm spin}$ is increased. However, quantitatively, the maps are virtually identical. Estimates of the H I column density however, will obviously suffer from the uncertainties imposed by this poor knowledge of $T_{\rm spin}$.

## IV. DISCUSSION

Here we will discuss the appearance and possible origins of the absorption over the range of observed velocities. Starting at high positive velocities, we see from Figure 1*c* that there is no absorption evident from any part of the field for positive velocities greater than $\sim 140$ km s$^{-1}$. The apparent *emission* from Sgr A* for high positive velocities (most pronounced for $280 \geq v \geq 250$ km s$^{-1}$ and $180 \geq v \geq 140$ km s$^{-1}$) is probably an artefact of the map-making process. Its origin may lie in the subtraction of the continuum map formed at one range of frequencies, from channel maps whose frequencies are not coincident with the continuum map frequencies.

Moving to the other end of the range, we see that at high negative velocities ($-220 \leq v \leq -160$ km s$^{-1}$) there is evidence of faint absorption against the compact point source Sgr A*, but from no other part of the field. Most of the interesting features occur within the velocity range $-140 \leq v \leq +140$ km s$^{-1}$ and some of these are discussed in the following subsections.

Before looking in detail at various features, we note that as well as the apparent emission from Sgr A*, referred to earlier, occurring in the high positive velocity channels, several of the more central channels also display white areas—again areas of apparent emission—which seem to outline some of the absorption features. The cause of this "emission" is almost certainly different to that proposed for the "emission" in the high positive velocity channels, and is most likely due to the lack of short spacings in our array (minimum baseline was 45 m). Such a lack would tend to produce a slight negative "bowl" around the areas of strong emission in the continuum map which would then appear as a positive "bowl" in the difference map.

We now discuss some of the features occurring across the range of observed velocities.

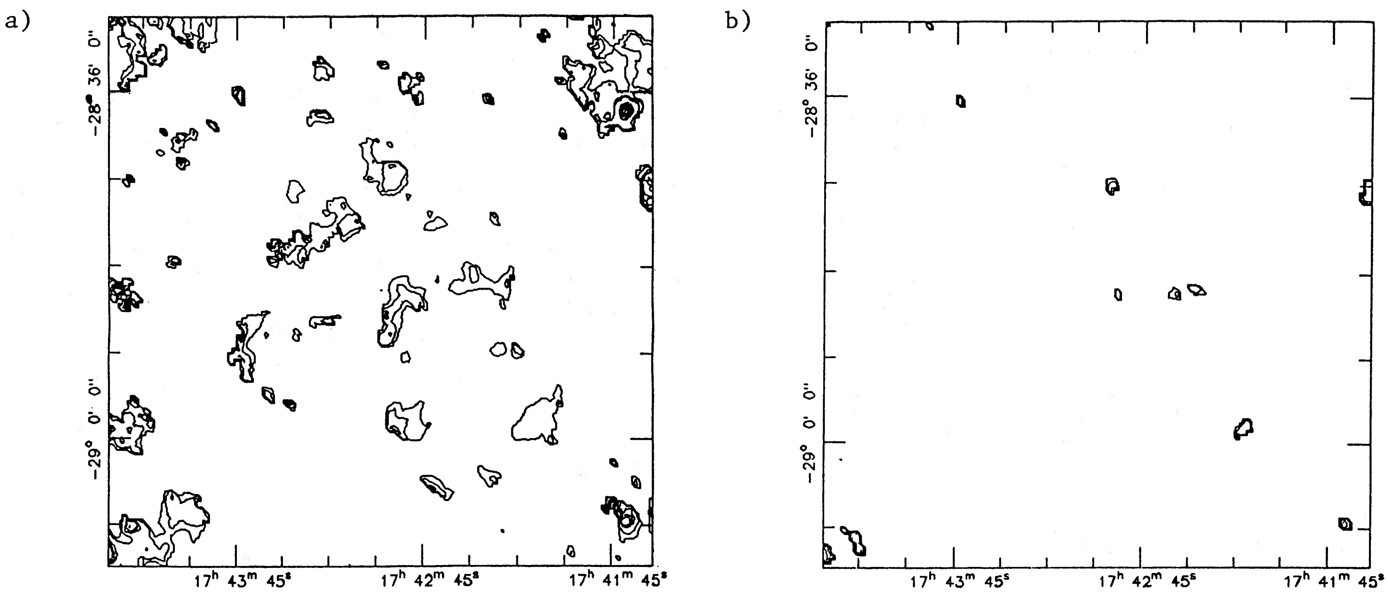


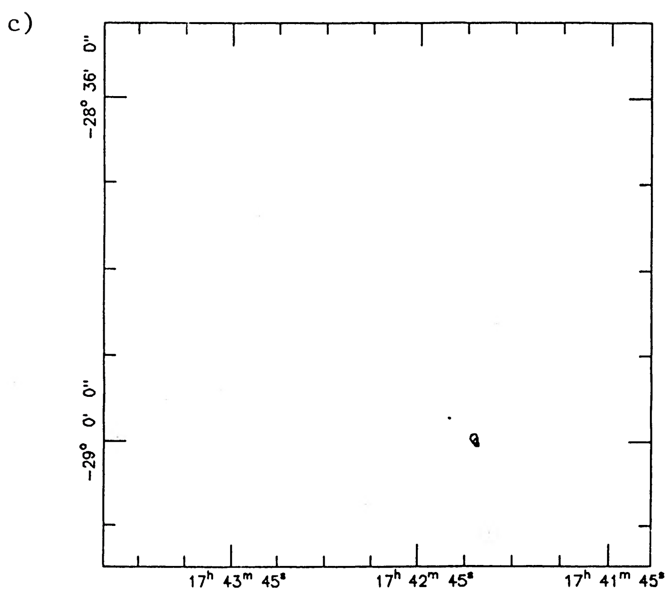


FIG. 2.—Comparison of three H I optical depth maps for one of the high positive velocity channels, centered on $\sim +196$ km s$^{-1}$. The maps were made using (*a*) a cutoff of 0.05 Jy beam$^{-1}$ in $I_c$. Contours of $\int_{\Delta v \simeq 10} \tau\, dv$ are 0.05, 0.2, 0.6, 0.8, 1.0, and 2.0 km s$^{-1}$. (*b*) cutoffs of 0.10 Jy beam$^{-1}$ in *both* $I_c$ and $|I_l - I_c|$. Contours of $\int_{\Delta v \simeq 10} \tau\, dv$ are 0.05, 0.1, 0.3, 0.6, 1.0, and 3.0 km s$^{-1}$. (*c*) the statistical technique outlined in § III. Contours of $\int_{\Delta v \simeq 10} \tau\, dv$ are 0.01 and 0.02 km s$^{-1}$.

### *a) +40 to 50 km s$^{-1}$ Material*

Figures 5*a* and 5*b* show maps of optical depth at +40 and +50 km s$^{-1}$, respectively, and it is apparent from these, and from Figure 1*c*, that there is *no* evidence of absorption against the Radio Arc or Arches at these velocities. The gas in front of the Sgr A complex is, however, well traced in Figures 5*a* and 5*b*. We are therefore faced with two alternatives: either the Arc lies in *front* of the 40 km s$^{-1}$ cloud, or the Arc lies behind (or in the vicinity), but the column density of the cloud drops off abruptly as the western end of the Arc is approached. To ensure that the absence of absorption is *not* due simply to a lack of gas over the region, it is necessary to estimate the column densities implied by CO and H I observations. Figure 1*b* of Liszt, Burton, and van der Hulst (1985) shows 3 cm continuum contours of the Arc overlaid onto contours of $T_A$*/0.65 (antenna temperature corrected for a beam efficiency of 0.65) in $^{12}$CO $J = 1 \rightarrow 0$ emission made with a 1′ beam and integrated over a 20 km s$^{-1}$ interval from +40 to 60 km s$^{-1}$. Values range from $\sim$160 to 480 K km s$^{-1}$ moving east-west across the Arc. Figure 6 shows contours of $^{13}$CO $J = 1 \rightarrow 0$ intensity integrated over a 10 km s$^{-1}$ interval from 40 to 50 km s$^{-1}$, made with a 100″ beam (taken from Bally *et al.* 1987), superposed onto the 20 cm continuum map of Figure 1*a*; we see that the values of $\int T_A^*\, dv$ range from $\sim$10 to 25 K km s$^{-1}$ across the Arc from east to west. Thus, correcting for beam efficiencies ($\sim$0.89 for the $^{13}$CO observations) and dividing by the velocity intervals gives average brightnesses, $T_{av}$, moving from east to west across the Arc, of

$$T_{av}(^{12}\mathrm{CO}) \text{ from 8 to 24 K}$$

and (4)

$$T_{av}(^{13}\mathrm{CO}) \text{ from 1.1 to 2.8 K}\ .$$

Note that we have ignored any effects introduced due to different beam sizes since the Arc is 3′–4′ across.

From the equation of radiative transfer one can write the observed $^{12}$CO peak antenna temperature, $T_A^*(^{12}\mathrm{CO})$, in terms of the excitation temperature of $^{12}$CO, $T_{ex}(^{12}\mathrm{CO})$;

$$T_A^*(^{12}\mathrm{CO}) = \eta_b \Phi \frac{h\nu_{12}}{k} \times [1 - \exp(-\tau_\nu)]\{f[T_{ex}(^{12}\mathrm{CO})] - f(T_{bb})\}\ , \quad (5)$$

where $\nu_{12}$ = frequency of the $^{12}$CO $J = 1 \rightarrow 0$ transition, $\eta_b$ = beam efficiency, $\Phi$ = filling factor, $f(T) = [\exp(h\nu/kT) - 1]^{-1}$, and $T_{bb} = 2.7$ K. (Here we are assuming that the major contribution to the background continuum at this frequency comes from the cosmic background radiation.)

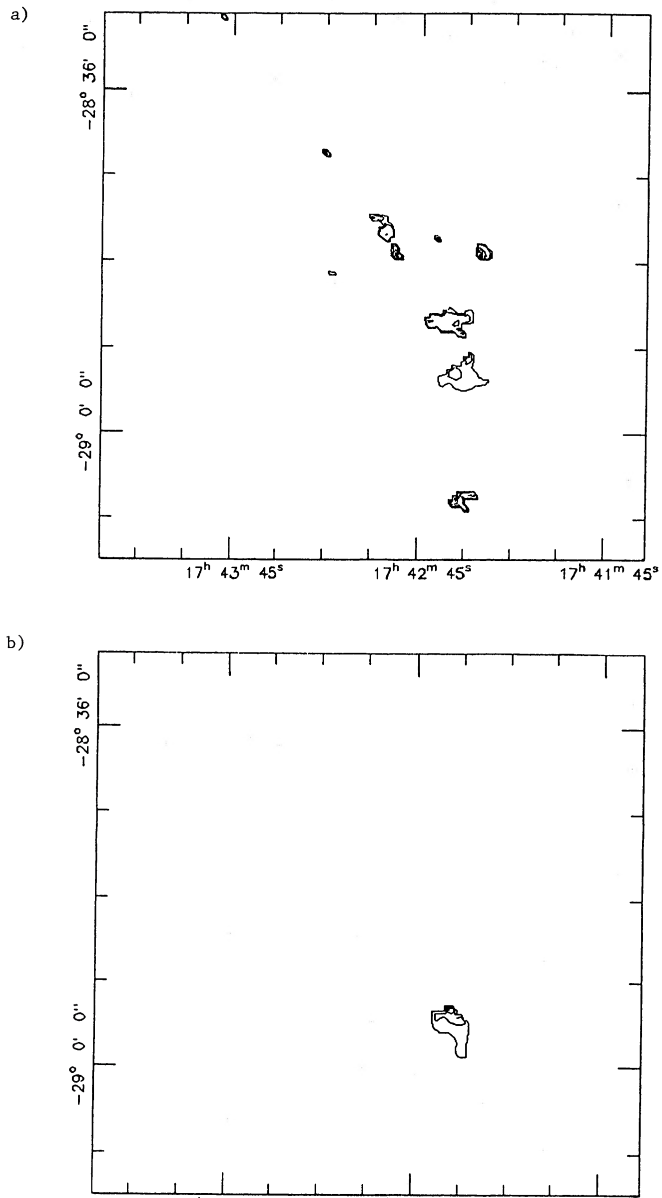


FIG. 3

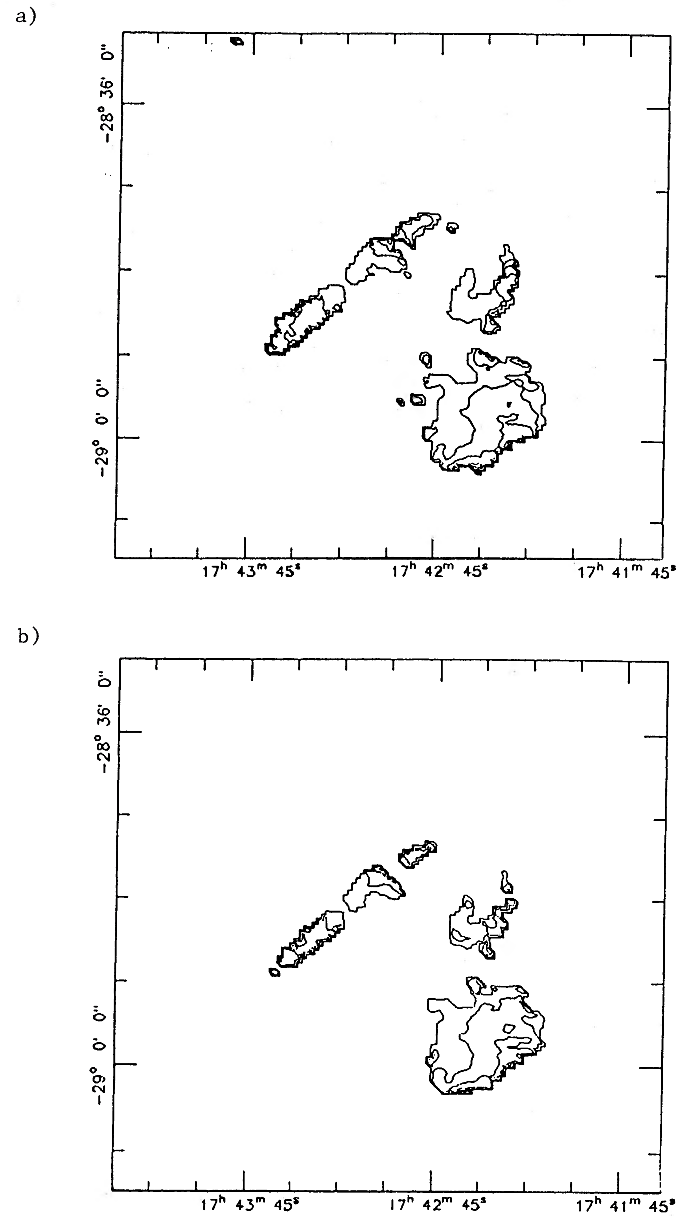


FIG. 4

FIG. 3.—Comparison of two H I optical depth maps for one of the high negative velocity channels, centered on $\sim -186$ km s$^{-1}$. The maps were made using (*a*) cutoffs of 0.10 Jy beam$^{-1}$ in *both* $I_c$ and $|I_l - I_c|$. Contours of $\int_{\Delta v \simeq 10} \tau\, dv$ are 0.05, 0.1, 0.3, 0.6, 1.0, 3.0, and 4.0 km s$^{-1}$. (*b*) the statistical technique outlined in § III. Contours of $\int_{\Delta v \simeq 10} \tau\, dv$ are 0.01, 0.05, 0.10, and 0.15 km s$^{-1}$.

FIG. 4.—Maps of H I optical depth for channel 30, centered on $\sim +21$ km s$^{-1}$. Both are made using the statistical technique outlined in § III, with (*a*) $T_{\rm spin} = 50$ K. Contours of $\int_{\Delta v \simeq 10} \tau\, dv$ are 0.13, 0.5, 1.0, 2.0, 2.5, and 2.8 km s$^{-1}$. (*b*) $T_{\rm spin} = 100$ K. Contours of $\int_{\Delta v \simeq 10} \tau\, dv$ are 0.14, 0.5, 1.0, 2.0, 2.5, and 2.8 km s$^{-1}$.

Since $^{12}$CO can be assumed to be optically thick, equation (5) can be used to obtain

$$T_{\rm ex}(^{12}{\rm CO}) = \frac{h\nu_{12}}{k} \ln\left\{1 + 1\Big/\left[\left(\frac{T_A{}^*k}{\Phi\eta_b h\nu_{12}}\right) + f(T_{\rm bb})\right]\right\} \quad (6)$$

An expression similar to equation (5) can be written for $T_A{}^*(^{13}{\rm CO})$ which can then be used to estimate $\tau_\nu(^{13}{\rm CO})$ as follows,

$$\tau_\nu(^{13}{\rm CO}) \simeq -\ln\left\{1 - \frac{kT_A{}^*(^{13}{\rm CO})}{\Phi\eta_b h\nu_{13}[f(T_{\rm ex}{}^{13}) - f(T_{\rm bb})]}\right\} . \quad (7)$$

where $\nu_{13}$ = frequency of $^{13}$CO $J = 1 \rightarrow 0$ line.

We can also write $\tau_\nu(^{13}{\rm CO})$ as

$$\tau_\nu(^{13}{\rm CO})\Delta v = \frac{c^3 g_2 A_{21} N_1}{8\pi g_1 \nu^3} [1 - \exp(-h\nu/kT_{\rm ex})] , \quad (8)$$

where $T_{\rm ex}$ now refers to $T_{\rm ex}(^{13}{\rm CO})$, $\Delta v$ = velocity interval under consideration and $N_1$ = column density of $^{13}$CO in level 1.

This expression can be rearranged to give $N_1$, and $N_1$ then converted to a *total* column density by assuming local thermodynamic equilibrium (LTE) and making an approximation to the partition function. Thus, assuming $T_{\rm ex}(^{12}{\rm CO}) \simeq$

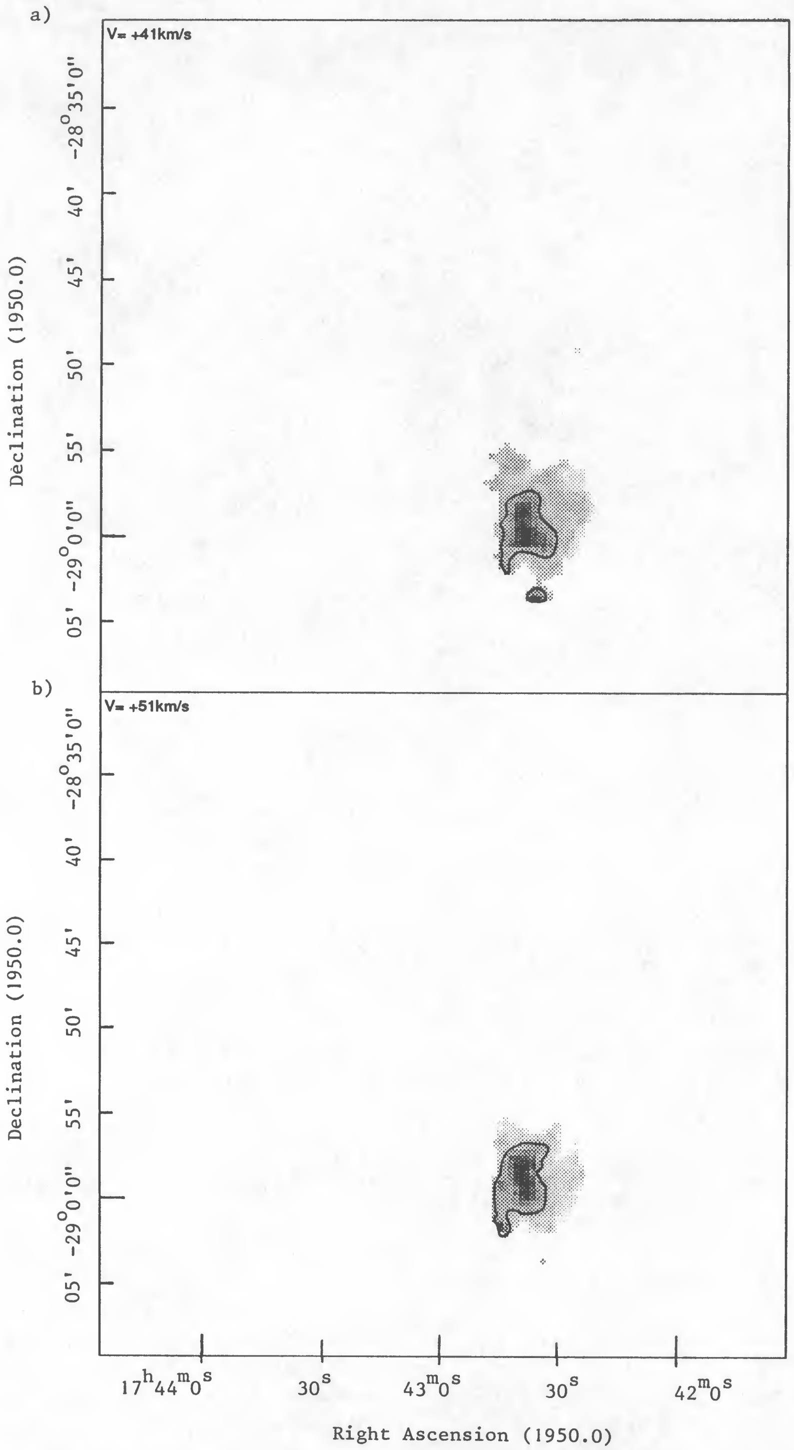


FIG. 5.—Gray-scale maps of H I optical depth centered on (*a*) about +41 km s$^{-1}$ and (*b*) about +52 km s$^{-1}$. In both cases the map scales are linear with $\int_{\Delta v \simeq 10} \tau\, dv$ ranging from 0(white) to 1.78 km s$^{-1}$(black) in (*a*) and from 0 (white) to 1.83 km s$^{-1}$(black) in (*b*). Contours on each map show the $\int_{\Delta v \simeq 10} \tau\, dv = 0.5$ level.

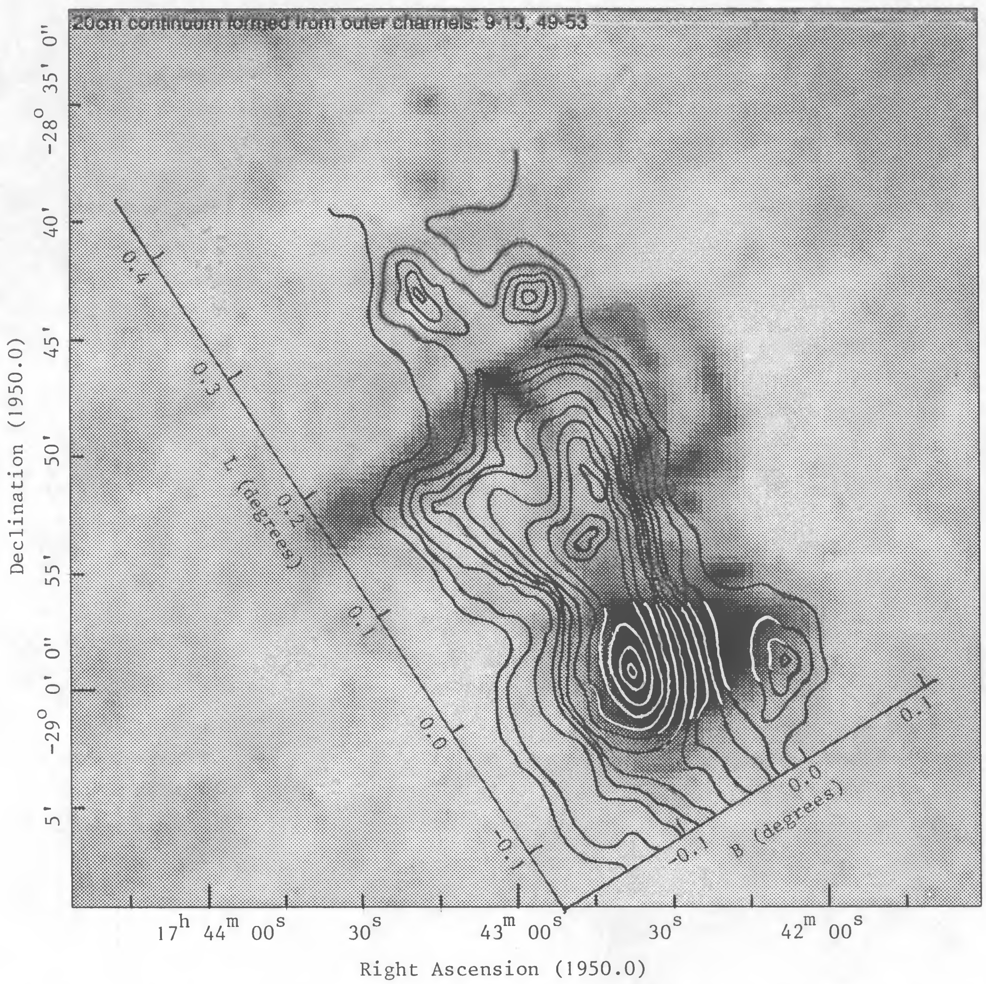


FIG. 6.—Contours show $^{13}$CO $J = 1 \rightarrow 0$ emission in the velocity range 40–50 km s$^{-1}$ (taken from Bally *et al.* 1987) over $|b| \leq 0.4$ and $-0.4 \leq l \leq 0.8$. Contour levels are 5, 7.5, 10, 12.5, 15, 20, 25, 27.5, 30, 32.5, 37.5, 40, and 42.5 K km s$^{-1}$. The gray-scale map is the 20 cm continuum taken from Fig. 1*a*. This figure illustrates the relation of the Galactic center radio structure to the molecular material at these velocities.

$T_{ex}(^{13}CO)$ (which will be approximately true in LTE) we can estimate the column density, $N$, of $^{13}$CO as follows

$$N(^{13}CO) \simeq \frac{3h\,\Delta v \tau_v(^{13}CO)}{8\pi^3\mu^2[\exp(h\nu_{13}/kT_{ex}) - 1]} \times \left(\frac{kT_{ex}}{hB} + \frac{1}{3} + \frac{hB}{15kT_{ex}}\right), \quad (9)$$

where $B$ = rotational constant for $^{13}$CO and $\mu$ = dipole moment.

For more detailed derivations of equations (5)–(9) see, for example, Lewtas (1987).

If we have a reliable conversion factor $\alpha$, where $N(H_2) = \alpha N(^{13}CO)$ it is then possible to make an estimate of the molecular hydrogen column density. If we use the locally determined value of the $H_2$:$^{13}$CO ratio, $\sim 10^6$ (Frerking, Langer, and Wilson 1982), the antenna temperatures given in equation (4) and equations (5)–(9), give the following $H_2$ column densities for the 40–60 km s$^{-1}$ material;

$$N(H_2) \simeq (1.1 \text{ to } 4.8) \times 10^{22} \text{ cm}^{-2}$$

per 10 km s$^{-1}$ bin.

The range represents the values obtained moving from east to west across the Arc.

It should be noted, however, that the $H_2$:$^{13}$CO ratio may be considerably different in the Galactic center region and will dominate the inaccuracy of the calculations.

H I optical depth is given by the following expression

$$\tau_v(\text{H I})\Delta v = \frac{c^3 g_2 A_{21} N_1}{8\pi g_1 \nu^3}[1 - \exp(-h\nu/kT_{spin})], \quad (10)$$

where $N_1$ is now the column density of H I in level 1, and other quantities are as described previously.

For the H I 21 cm line we assume that $N_1(\text{H I}) = N(\text{H I})/4$ and that $[1 - \exp(-h\nu/kT_{spin})] \simeq h\nu/kT_{spin}$, so that equation (10) can be written as

$$\tau_v(\text{H I})\Delta v\ (\text{km s}^{-1}) \simeq 5.49 \times 10^{-19}\,\frac{N_{col}(\text{H I})\ (\text{cm}^{-2})}{T_{spin}}. \quad (11)$$

Thus, using $N(\text{H I}) = \beta N(H_2)$ and $\beta \simeq 0.01$ (see Liszt *et al.* 1983) we have

$$\Delta v \tau_v(\text{H I}) \simeq 5.49 \times 10^{-21}\,\frac{N(H_2)}{T_{spin}} \quad (12)$$

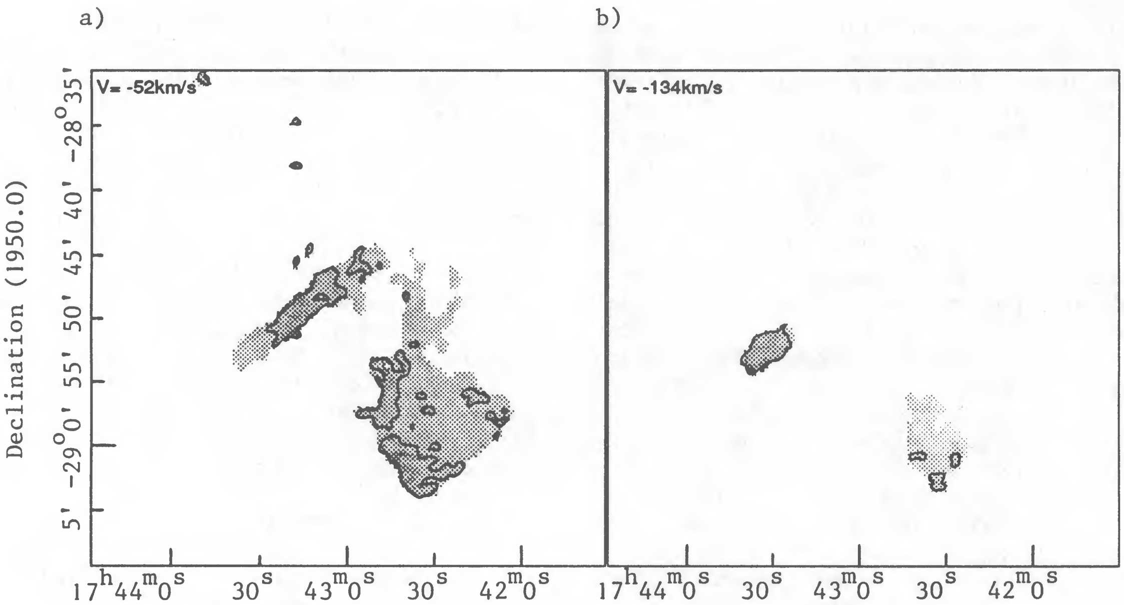


FIG. 7.—(*a*) Gray-scale map of H I optical depth for channel 37, centered on about $-52$ km s$^{-1}$. The map scale is linear with $\int_{\Delta v \simeq 10} \tau \, dv$ ranging from 0(white) to 2.66 km s$^{-1}$(black). Contour shows the $\int_{\Delta v \simeq 10} \tau \, dv = 0.8$ level. (*b*) Gray-scale map of H I optical depth for channel 45, centered on about $-134$ km s$^{-1}$. The map scale is linear with $\int_{\Delta v \simeq 10} \tau \, dv$ ranging from 0(white) to 1.75 km s$^{-1}$(black). The contour shows the $\int_{\Delta v \simeq 10} \tau \, dv = 0.2$ level. Here we are seeing the southern portion of the Radio Arc being absorbed by the front section of the "expanding molecular ring" feature at $R \sim 200$ pc (see § IV*e*).

While Liszt *et al.* (1983) point out that a value of $N$(H I):$N(H_2) \simeq 0.01$ is that required for H I self-absorption at higher Galactic longitudes, we should note that there is a good deal of uncertainty attached to the value of $\beta$. Taking $\beta \sim 0.01$, $T_{\rm spin} \lesssim 100$ K and using the range of $N(H_2)$ given previously we see that

$$\tau \, \Delta v \geq 0.60 \text{ km s}^{-1} .$$

Under these assumptions one might therefore expect to see $\tau \, \Delta v$ values over the interval 40–50 km s$^{-1}$ of the order of 0.60 km s$^{-1}$. Figures 5*a* and 5*b* show that no $\tau$ is observed greater than $\sim$0.05 km s$^{-1}$.

While designed to illustrate that CO observations would seem to imply a column density of H I sufficient to produce significant absorption of the Radio Arc, the above argument is rendered somewhat inconclusive by the large uncertainties in quantities such as $\alpha$, $\beta$, and $T_{\rm spin}$. However, if one makes similar analyses on other bodies of gas which *do* absorb the Arc—e.g., the $-50$ km s$^{-1}$ material or the $-130$ km s$^{-1}$ gas (shown in Fig. 7*a* and 7*b*)—it is found that the $\tau$ maps *do* show contours across the Arc at the expected levels. This fact therefore gives us confidence in concluding that the 40 km s$^{-1}$ cloud lies wholly *behind* the Radio Arc.

Liszt *et al.* (1985) have proposed that, given the correlation between the $^{12}$CO 40 to 60 km s$^{-1}$ data and the radio continuum (see Liszt *et al.* 1985, Figure 1*b*), the continuum may originate in a shell or cocoon around the neutral cloud. The H I absorption observations presented here do not lend support to this theory and, moreover, suggest that despite past evidence of Arc–40 km s$^{-1}$ cloud interactions, the Arc and this molecular cloud appear *not* to be related in an intimate way; although our observations cannot rule out an interaction occurring at the western edge of the Arc if the 40 km s$^{-1}$ cloud ends abruptly here. Similarly, Bally *et al.* (1988) have argued that the coincidence of the "edge" of the 40 km s$^{-1}$ cloud with the nonthermal Radio Arc suggests that the Arc filaments may have been produced by shocks caused by the passage of a dense molecular cloud in a highly eccentric orbit, through lower density gas in the plane of the Galaxy. While this is a rather appealing explanation of the observed structure, it may be difficult to see why, if the filaments are indeed produced by such a collision as the 40 km s$^{-1}$ gas streams toward higher $b$ values, we do not observe the Arc in absorption from the non-shocked material.

Thus, while on the one hand there appears to be good evidence for 40 km s$^{-1}$ cloud–Arc interaction, as witnessed by the $NH_3$ emission (Güsten *et al.* 1981) and recombination line studies (Pauls and Mezger 1980) described earlier, on the other hand, the H I absorption measurements give no indication at all of such an interaction. The lack of absorption at 40–50 km s$^{-1}$ cannot, of course, wholly rule out the situation in which the 40 km s$^{-1}$ cloud lies immediately behind the Arc but does interact with the Arc in some way.

### *b) +20 km s$^{-1}$ Material*

As we move from larger to smaller positive velocities, the Arc first appears in absorption around +20 km s$^{-1}$ (see Fig. 1*c*). The optical depth map at +20 km s$^{-1}$ of Figure 8 shows that while the 20 km s$^{-1}$ material apparently covers the northern and southern tips of the Arc, there is a central gap just below G0.18−0.04 where there is little or no gas. Figure 9*a* shows the $^{13}$CO $J = 1 \rightarrow 0$ map at 20–30 km s$^{-1}$ (taken from Bally *et al.* 1987) overlaid onto the 20 cm continuum map of Figure 1*a*, and it is clear from this that there exist two condensations in the cloud relevant to the northern and southern areas of absorption observed in our data. The northern condensation ($l \simeq 0\overset{\circ}{.}2$, $b \simeq -0\overset{\circ}{.}03$) corresponds almost exactly with the absorption peak in this region, while the material from the southern condensation ($l \simeq 0^{\circ}.12$, $b \simeq 0^{\circ}.11$) may be linked with the southern absorption peak. It is also interesting to note that the single dish recombination line study of Pauls and Mezger (1980) showed emission at around $+20$ km s$^{-1}$ covering the sickle and northern Arc which is apparently centered eastward of the Arc. This might therefore lead us to believe that the neutral gas, as seen in H I absorption, the molecular gas traced by $^{13}$CO (Bally *et al.* 1987) and the ionized material (Pauls and Mezger 1980) at $+20$ km s$^{-1}$ are physically related. In addition to this, there is also evidence of H110$\alpha$ recombination line emission at $+20$ to 30 km s$^{-1}$ over the sickle feature from higher resolution VLA observations (YZ86), and recent H78$\alpha$ emission observations made at Green Bank (Anantharamaiah and Yusef-Zadeh 1989) show that some of the more diffuse material surrounding the Radio Arc and associated with the helical filaments also has a velocity around $+20$ km s$^{-1}$. It should be noted here that this material at 20 km s$^{-1}$ does not appear to be connected with the 20 km s$^{-1}$ material seen in the SW of the Sgr A complex, which has been called the "20 km s$^{-1}$ cloud" by various authors. Another intriguing feature is the correlation between the 3 cm polarized emission, shown in solid contours (Seiradakis *et al.* 1985*b*), and the H I optical depth at $+20$ km s$^{-1}$ which is illustrated in Figure 9*b*. The 3 cm map shows three distinct regions of polarization; two of these are from large lobes past the north and south ends of the Arc, and the third, marked as source A, is from the central Arc just below G0.18 − 0.04. We see that the central region coincides almost exactly with the gap in the 20 km s$^{-1}$ H I optical depth. This therefore suggests a scenario in which the filaments of the Arc are entirely nonthermal in nature, but suffer from the depolarization of most of their synchrotron emission by ionized material associated with the $+20$ km s$^{-1}$ gas. A natural consequence of this would then be that it is the 20 km s$^{-1}$ gas which is intimately related to the Arc instead of, or as well as, the 40 km s$^{-1}$ cloud.

In this context it is interesting to look at the results of other recent polarimetric observations of the Galactic center region by Sofue *et al.* (1987, hereafter S87) at 5 GHz and by Inoue *et al.* (1984, hereafter I84) at 10 GHz. Both sets of observations reveal polarization structures over the Radio Arc similar to the 10 GHz data of Seiradakis *et al.* (1985*a*), but there appear to be significant differences in position and rotation measure (RM) between the 5 and 10 GHz peaks on the Arc.

The broken contours in Figure 9*b* show polarized intensity at 5 GHz (from S87), and it is clear that the peak of the polarized emission on the Arc at 5 GHz (source A′) is displaced to the southeast of that at 10 GHz (source A). Source A′ lies in a region of greater H I optical depth than does source A, but the values of $\tau$(H I) in this region are still much smaller than those at the peak, which occurs toward the southern end of the Arc.

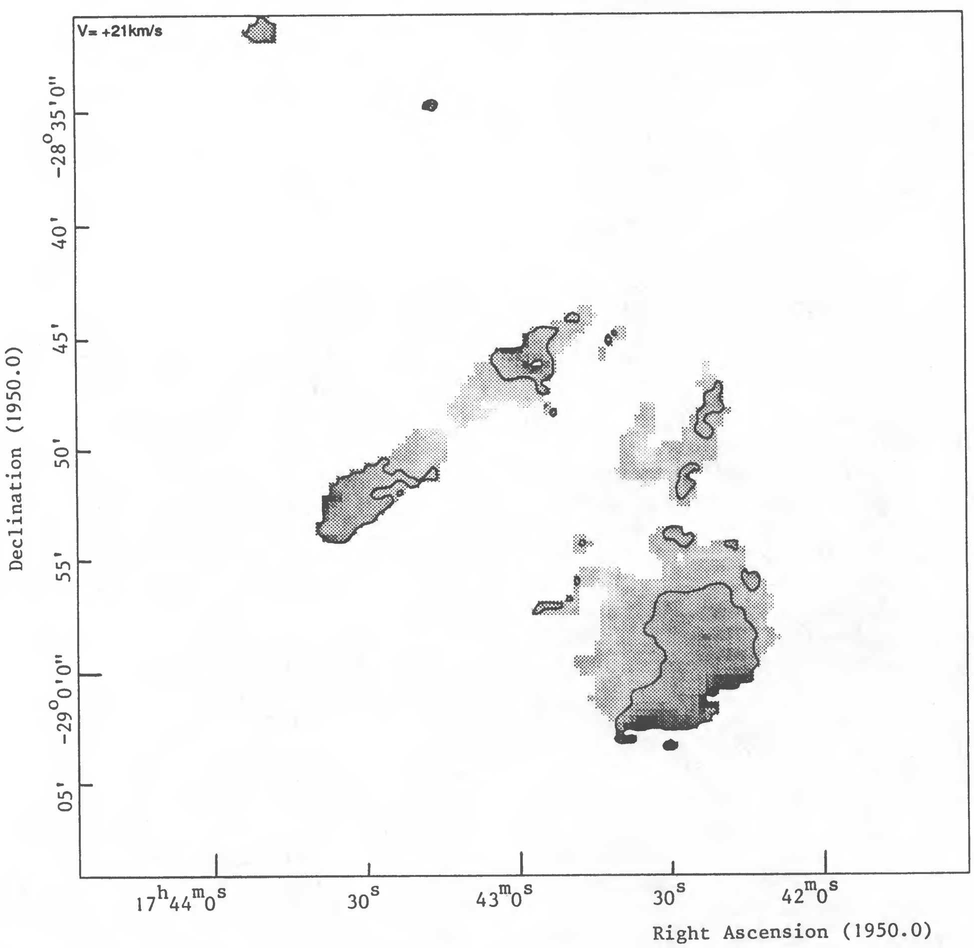


FIG. 8.—Gray-scale map of H I optical depth for channel 30, centered on about $+21$ km s$^{-1}$. Map scale is linear, with $\int_{\Delta v \simeq 10} \tau\, dv$ ranging from 0 to 2.67 km s$^{-1}$. The contour shows the $\int_{\Delta v \simeq 10} \tau\, dv = 0.5$ level. Note the apparent "gap" in the 20 km s$^{-1}$ material across the central section of the Arc.

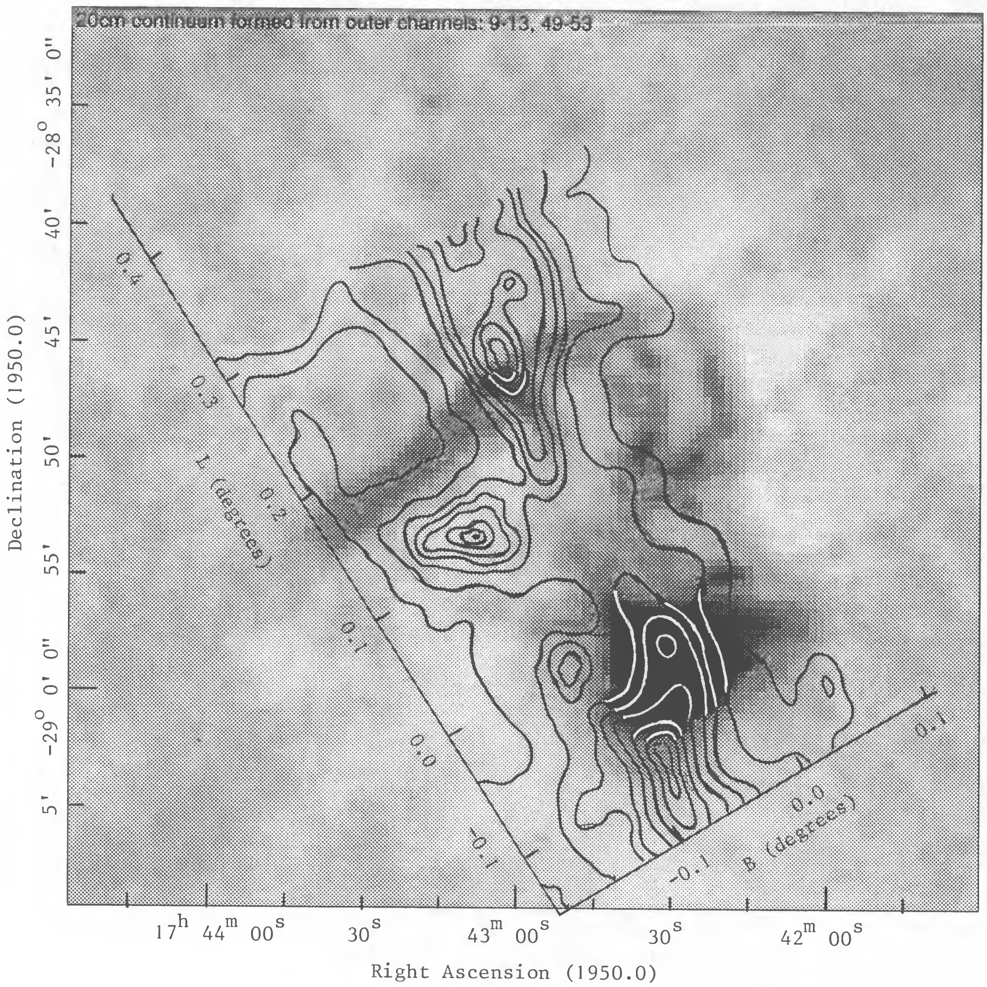


FIG. 9a

FIG. 9.—(*a*) Contours show $^{13}$CO $J = 1 \rightarrow 0$ emission over the velocity interval 20–30 km s$^{-1}$ (taken from Bally *et al.* 1987). Levels are set at 5, 10, 20, 22.5, 25, 35, 37.5, and 40 K km s$^{-1}$. The gray scale is the 20 cm radio continuum emission of Fig. 1*a*. (*b*) The gray-scale map of the 20 km s$^{-1}$ material of Fig. 8 is shown here overlaid with maps of 3 cm *polarized* emission (*solid contours*) taken from Seiradakis *et al.* (1985*b*), and 6 cm *polarized* emission (*dashed contours*) taken from Sofue *et al.* 1987; A and A′ mark the peaks of the 3 cm and 6 cm polarized emission on the Arc. (*c*) $^{12}$CO $J = 2 \rightarrow 1$ spectrum taken at $\alpha = 17^h43^m9^s.6$, $\delta = -28°47'8''.0$, lying at a point in the Arc at which the H I optical depth at $\sim 20$ km s$^{-1}$ is large. The temperature scale is $T_A$*. The spectrum was kindly taken for us during commissioning of the James Clerk Maxwell Telescope by R. Padman and N. Parker.

Source A is polarized at 10 GHz by $\sim 10\%$ and has a large *negative* RM, but shows very little ($<0.5\%$) polarization at 5 GHz; source A′, however, is $\sim 1\%$ polarized at 5 GHz and has a large *positive* RM, but shows no ($<0.5\%$) polarization at 10 GHz. While the degree of polarization displays this strange behavior, the variation of the polarization angle, $\chi$, at both 5 and 10 GHz does appear to follow approximately a $\lambda^2$ law.

We will now look in more detail at sources A and A′.

i) *Source A*

In a mixed thermal and synchrotron emitting region, depolarization will occur, and the relevant formulae were established in a classic paper by Burn (1966). Here, Burn predicted the degree of depolarization, $p$, and the polarization angle, $\chi$, for some specialized geometries (slab and sphere). For a slab he found that $p \propto |\sin \delta|/\delta$, where $\delta \simeq \lambda^2$RM, so that $p$ decreases to zero at $\delta = n\pi$. I84 attribute their observed RM and rapid decrease of $p$ as $\lambda$ goes from $\sim 2.8$ to $\sim 3.3$ cm to a $p \propto |\sin \delta|/\delta$ behavior. However, as pointed out by Laing (1984) one should be cautious about applying the results of Burn (1966) to realistic geometries, in which a general trend of decreasing $p$ with increasing $\lambda$ will probably prevail, but no such $\sin \delta/\delta$ behavior will be likely. Since both decreasing $p$ with increasing $\lambda$ *and* a $\lambda^2$ dependence of $\chi$ are observed in source A, the cause could be a foreground (or associated) screen, internal depolarization, or a mixture of both.

ii) *Source A′*

Source A′ apparently violates the trend of decreasing polarization with increasing wavelength. Here we will discuss three possible explanations of the observed anomalous polarization behavior.

1. The first is that proposed by S87, who explain this anomaly again by reference to the specialized geometries of Burn, attributing the observed reversal in RM to the change in sign which occurs as $\lambda$ passes through the value at which $p$ is zero, and the polarization differences betwen A and A′ to a possibly complex dependence of $p$ on frequency. The major drawback of this explanation is the need to invoke special geometries to explain the strange behavior of the polarization

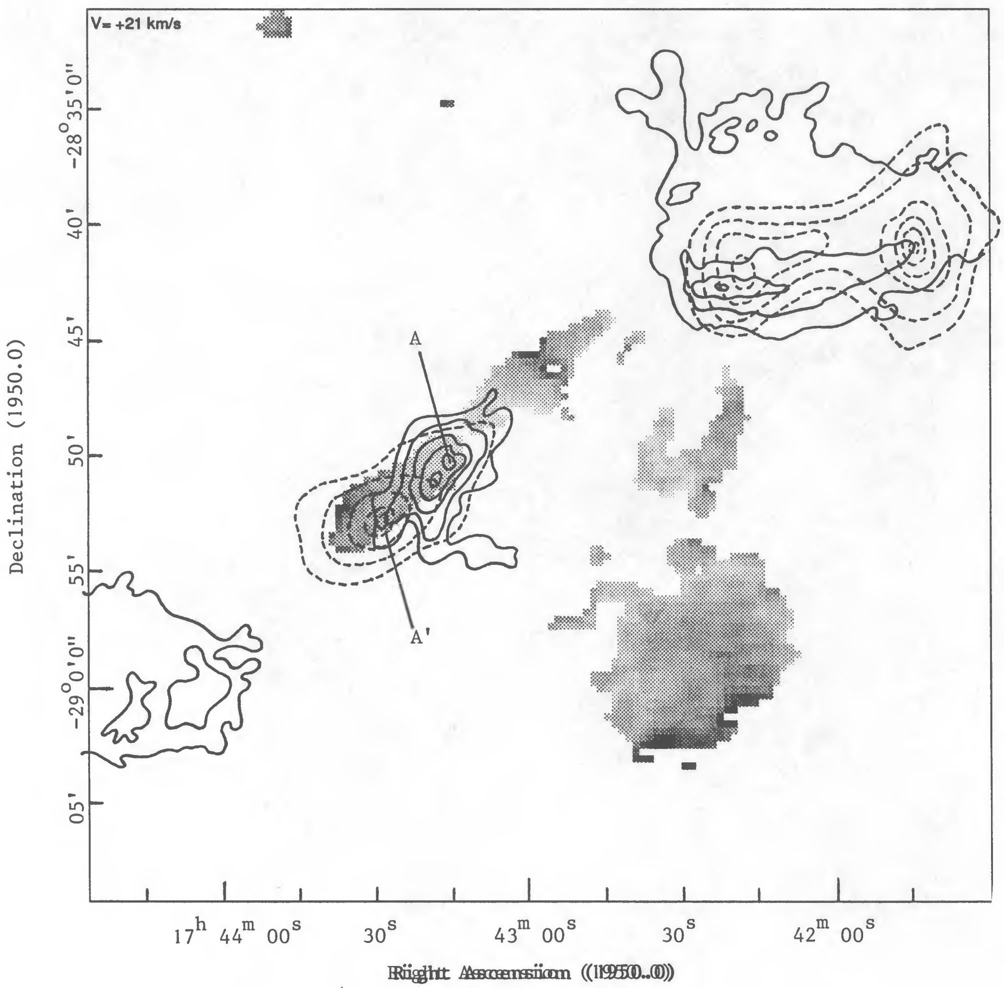
V= +21 km/s
A
A'
−28°35'0"
40'
45'
50'
55'
−29°0'0"
05'
Declination (1950.0)
17h 44m 00s
30s
43m 00s
30s
42m 00s
Right Ascension (1950.0)

FIG. 9b

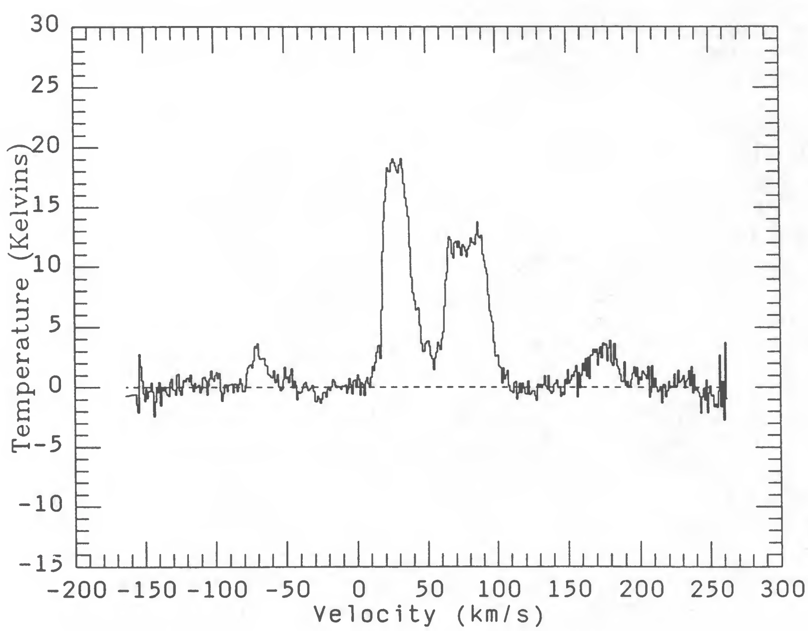
Temperature (Kelvins)
Velocity (km/s)

FIG. 9c

characteristics, while there is no obvious observational evidence for such geometries, nor for the required complicated dependences of $p$ and $\chi$ on $\lambda$.

2. Alternatively, one can envisage a special geometry in which a helical-shaped magnetic structure surrounds (wraps around) the straight filaments of the Arc. It would then be possible to see a superposition of different field directions along a given line of sight, which could lead to the observed reversal in RM. Such helical structures are clearly visible in the 20 cm map of Figure 1*a* (see also Yusef-Zadeh *et al.* 1984), and moreover, recent 2 cm polarization measurements (Inoue *et al.* 1989) reveal a polarized section of one such helical feature where it crosses the linear filaments.

3. The third scenario is that in which the 20 km $s^{-1}$ gas may be closely associated with the Radio Arc and may fuel an ionized, inhomogeneous medium surrounding the Arc—this medium would completely depolarize the synchrotron emission from the nonthermal Arc filaments where the 20 km $s^{-1}$ gas is densest. The absence of polarized emission from those parts of the Arc covered by the densest parts of this cloud supports this picture. Source A, observed to be strongly polarized at 10 GHz, occurs in a region of the Arc where there is a very low column density of gas at 20 km $s^{-1}$. The observed $\lambda^2$ dependence of $\chi$ and rapid decrease of $p$ with increasing $\lambda$ could be attributed to a mixture of internal Faraday depolarization and depolarization by a foreground screen. This screen would be a more diffuse component connected to the depolarizing medium and fueled by the 20 km $s^{-1}$ cloud.

Source A′ is only $\sim 1\%$ polarized at 5 GHz, and this smaller value of $p$ may occur as A′ lies in a region of slightly greater 20 km $s^{-1}$ H I optical depth. How then, is the lack of polarization from source A′ at 10 GHz explained?

Burn (1966) points out that spatial variations of the emission spectrum and state of polarization can also produce variations of the observed $p$ with wavelength. The beams used for the 5(S87) and 10 GHz(I84) observations were similar at $\sim 2\overset{'}{.}44$ and $2\overset{'}{.}7$, respectively, and thus, one beamwidth covers almost the whole width of the Radio Arc. We will show below that it is possible to produce the observed *decrease* in polarization with a *decrease* in $\lambda$ if the radio continuum in the beam varies in an appropriate way, while still preserving a $\lambda^2$ dependence of $\chi$.

We first suppose that the depolarization is due to differing values of $p$ and $\alpha$ (spectral index, $S \propto \nu^{-\alpha}$) within the beam while $\chi$ remains constant. The polarization across the beam is then given by

$$P = \exp(2i\chi)\,\frac{\int_{\text{source}} k(\boldsymbol{r})\nu^{-\alpha(\boldsymbol{r})}p(\boldsymbol{r})dx\,dy}{\int_{\text{source}} k(\boldsymbol{r})\nu^{-\alpha(\boldsymbol{r})}\,dx\,dy}\,, \tag{13}$$

where the flux $S$ is given by $S(\boldsymbol{r}) = k(\boldsymbol{r})\nu^{-\alpha(\boldsymbol{r})}$ and we have written the complex linear polarization as $P = p(\boldsymbol{r}) \exp(2i\chi)$ (following Burn 1966). For illustration, we consider one-dimensional gradients across the width of the Arc as the different filaments are traversed, and we will also assume that there exists a frequency $\nu_0$ such that at $\nu = \nu_0$ there is no flux variation across the source, i.e., $S = S_0(\nu/\nu_0)^{-\alpha(\boldsymbol{r})}$ with $S_0$ constant; this enables us to work with the dimensionless quantity $(\nu/\nu_0)$. If $x$ is the distance across the Arc, then from $x = 0$ to $L$ (width of the Arc in suitable units) we choose the following variations

$$k(x) = k\,, \qquad \text{constant}$$

$$\alpha(x) = \delta + \mu x\,, \quad \mu < 0\,,$$

$$p(x) = g(x)\,.$$

Calculations have shown that to give the observed rapid decline in $P$ from 5 to 10 GHz, it is necessary to choose a function $g(x)$ which produces a fairly steep decrease in $p$ for $x$ increasing from 0 to $L$. We therefore choose

$$g(x) = \exp(-\beta x)\,, \quad \beta > 0\,.$$

Thus, $P$ can be written as

$$P = \exp(2i\chi)$$

$$\times \left\{\left[\int_0^L \exp(-\beta x)\left(\frac{\nu}{\nu_0}\right)^{-\mu x} dx\right]\Big/\left[\int_0^L \left(\frac{\nu}{\nu_0}\right)^{-\mu x} dx\right]\right\}. \tag{14}$$

Putting $\gamma = -\mu \ln(\nu/\nu_0)$ so that $\exp(\gamma x) = (\nu/\nu_0)^{-\mu x}$ gives

$$P = h(\omega)\exp(2i\chi)\,, \tag{15}$$

where

$$h(\omega) = \frac{\omega}{\omega - a}\,\frac{[\exp(\omega - a) - 1]}{[\exp(\omega) - 1]} \quad \text{and} \quad \omega = \gamma L\,, \quad a = \beta L\,.$$

For $\mu < 0$ and $\beta > 0$ $h(\omega)$ is a monotonically decreasing function of $\omega$ for $\omega$ positive. Thus, $P$ decreases as $\nu$ increases as required. The ratio $P(10\text{ GHz}){:}P(5\text{ GHz})$ can be made to be less than 0.5 (as observed) for spectral index changes greater than $\sim 1.5$ and for values of $a$ which produce a moderately steep increase in $p(x)$ as $x$ increases. For example, with $a = 10$ and $\nu_0 = 1.25$ GHz, $(P_{10}/P_5) < 0.5$ for $|\Delta\alpha| \gtrsim 1.7$ ($\Delta\alpha =$ change in spectral index across the Arc).

One must, of course, note here that such values of $a$ and $\nu_0$ may not be applicable to the real situation, and that such a large change in $\Delta\alpha$ would be surprising. However, while the above example is obviously a very specialized case, it does illustrate that, in theory, it seems possible to account for the observed decrease in $p$ with increasing $\nu$, by assuming variations of $p$ and $\alpha$ within the beam. Recent work on the spectral index variation across the Arc by Reich *et al.* (1987) finds that over one region of the southern part of the Arc, the less intense regions of polarized emission have a flatter spectrum. The derived values of $\alpha$ are due to *both* thermal and nonthermal emitting material, and via a decomposition, Reich *et al.* infer from this data that the nonthermal component has an inverted spectrum with $S \propto \nu^{0.3}$. This is encouraging since the $\Delta\alpha$ required to produce $(P_{10}/P_5) < 0.5$ in the previous explanation, would probably produce an inverted spectrum. However, the observed changes in spectral index, $\alpha$, over the Arc region do not appear to be capable of providing the relatively large change in $\alpha$ required to explain the polarization anomaly.

To summarize, it is proposed here that the observed spatial distribution of the polarized intensity of the Galactic center Radio Arc is attributable mainly to an associated depolarizing medium which is closely connected to the 20 km $s^{-1}$ molecular gas. The cause of the apparent anomalous behavior of $p$ with frequency over source A′ is presently unclear, but may possibly be explained by some combination of the three mechanisms discussed above.

If one is to believe that the $\sim 20$ km $s^{-1}$ gas is closely associated with the Arc, it is obviously important to try to show that the material is not simply a line of sight feature. There are several arguments which point toward this cloud lying close to the Galactic center.

First, the formaldehyde absorption observations of Güsten and Downes (1980), revealed a cloud at around $+25$ km $s^{-1}$ across the northern portion of the Radio Arc and coinciding with the upper section of the H I cloud at 20 km $s^{-1}$. They estimate that this cloud is fairly dense, has a mass of $\sim 4 \times 10^5$ $M_\odot$ (using $D_{gc} = 10$ kpc), and displays line widths of $\sim 30$ km $s^{-1}$—characteristics of Galactic center clouds rather than of normal disk clouds. From our H I observations we can put a crude lower limit (because we see only that portion of the cloud in front of the continuum) on the mass of the cloud at 20 km $s^{-1}$ across the northern section of the Arc; $M_{cloud} \gtrsim 6 \times 10^4$ $M_\odot$ (using $D_{gc} = 8.5$ kpc) or $M_{cloud} \gtrsim 8 \times 10^4$ $M_\odot$ (using $D_{gc} = 10$ kpc).

Second, Figure 9*c* shows a $^{12}$CO $J = 2 \rightarrow 1$ spectrum taken at $\alpha = 17^h43^m9\overset{s}{.}6$, $\delta = -28°47'8\overset{''}{.}0$, a point on the Arc where the H I optical depth at $\sim +20$ km $s^{-1}$ is large. The large line width of the $+20$ km $s^{-1}$ feature shown here ($\Delta v_{FWHM} \simeq 25$ km $s^{-1}$) again suggests that the 20 km $s^{-1}$ material lies in the vicinity of the Galactic center. However, more convincing evi-

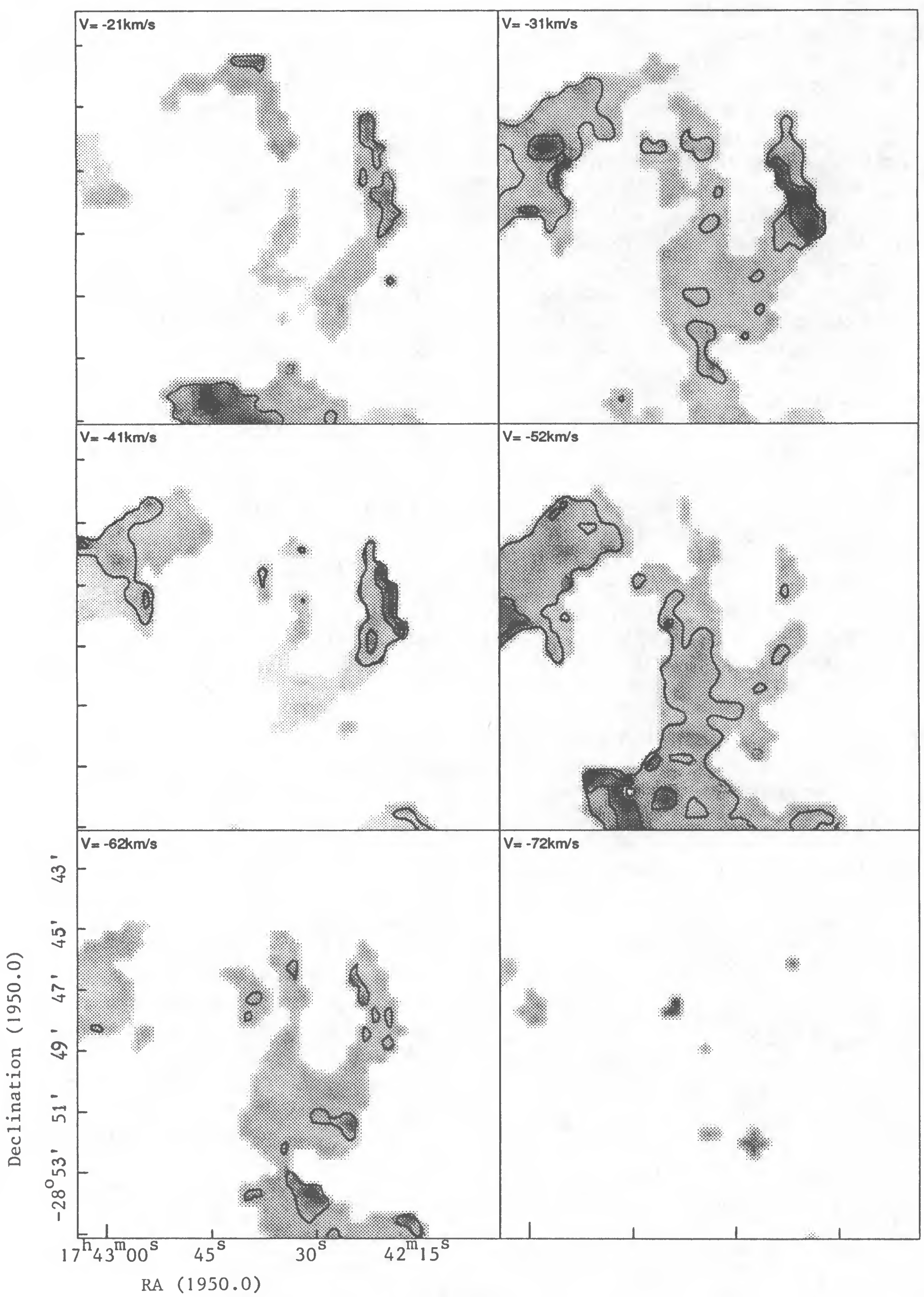


FIG. 10.—Maps of H I optical depth over the arched filaments for six negative velocity channels. In each map the scale is linear, and the ranges of $\int_{\Delta v \simeq 10} \tau\, dv$ are 0–1.3 km $s^{-1}$ ($-20$ km $s^{-1}$ material), 0–1.7 km $s^{-1}$ ($-30$ km $s^{-1}$ material), 0–2.05 km $s^{-1}$ ($-40$ km $s^{-1}$ material), 0–1.82 km $s^{-1}$ ($-50$ km $s^{-1}$ material), 0–1.20 km $s^{-1}$ ($-60$ km $s^{-1}$ material), and 0–0.37 km $s^{-1}$ ($-70$ km $s^{-1}$ material). In each frame contours of $\int_{\Delta v \simeq 10} \tau\, dv = 0.5$ and 1.0 are marked.

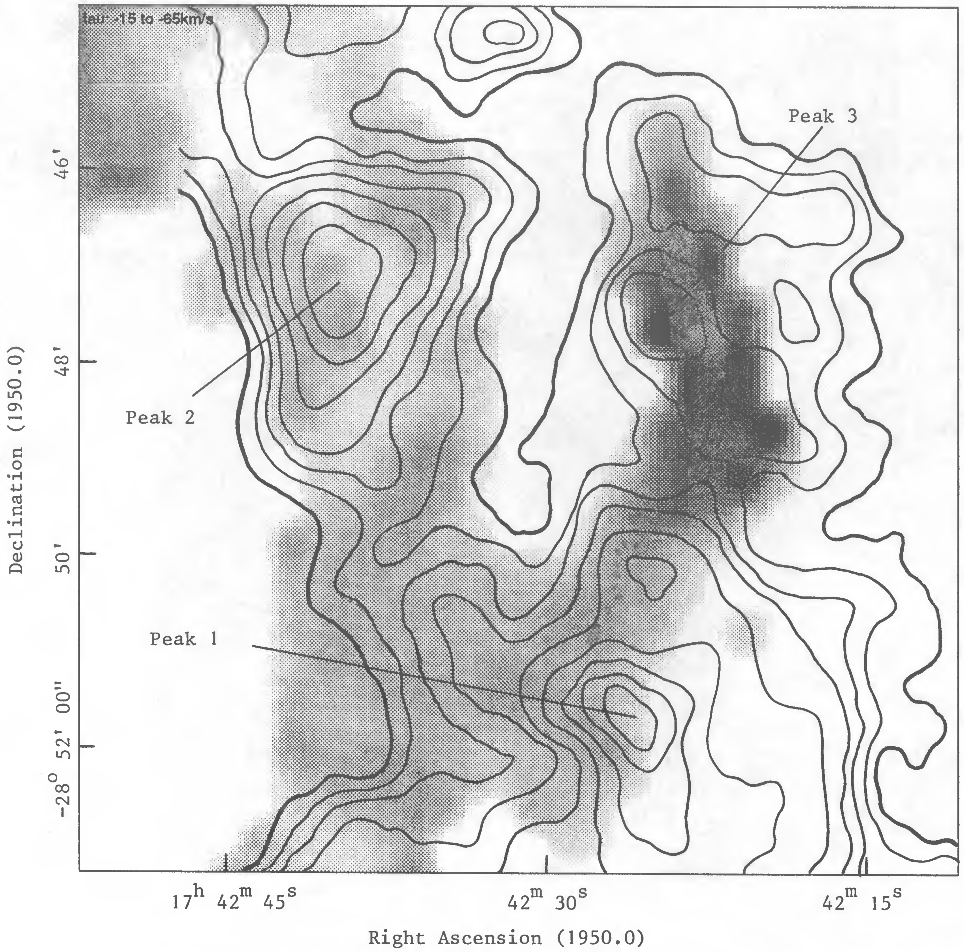


FIG. 11.—Contours of CS $J = 2 \rightarrow 1$ emission in the range $+5$ to $-55$ km s$^{-1}$ (taken from Serabyn and Güsten 1987) across the arched filaments, overlaid onto a gray scale of H I optical depth integrated over a 50 km s$^{-1}$ velocity interval between $-15$ and $-65$ km s$^{-1}$ [$\int_{-65}^{-15} \tau(\mathrm{H\ I})dv$]. The optical depth map scale is linear and ranges from 0 to 4.21 km s$^{-1}$. The CS contour levels are 10, 14, 18, 22, 30, 40, 50, 60, and 70 K km s$^{-1}$.

dence would be spectra from a molecule such as CS which traces dense gas and is less likely to have a line-of-sight origin.

### *c) $-10$ to $-60$ km s$^{-1}$ Material: Arched Filaments*

Far-infrared (FIR) and radio recombination line data (Dent *et al.* 1982; YZ86; Pauls and Mezger 1980) have shown that the arched filaments, or Arches, occurring at $\alpha = 17^{\mathrm{h}}42^{\mathrm{m}}30^{\mathrm{s}}$ and $\delta \sim -28°48'$, appear to be predominantly thermal structures. There is also substantial evidence that molecular material in the negative velocity range 0 to $-60$ km s$^{-1}$ is closely associated with the thermal Arches (YZ86; Bally *et al.* 1987; Serabyn and Güsten 1987, hereafter SG87). In particular, high-resolution CS $J = 2 \rightarrow 1$ mapping of the Arches region (SG87) shows clearly that the bulk of the molecular gas appears to be both spatially and kinematically associated with the ionized filaments.

H I optical depth maps of the Arches for velocity channels centered on $-21$ to $-62$ km s$^{-1}$, as seen in Figure 10, show an overall correlation in velocity with the kinematic structure observed in the molecular and ionized gas (YZ86; SG87). The velocity distribution of the H I gas in front of the Arches is such that the more negative velocity gas is observed toward the western end of the Arches, closest to Sgr A (this is seen particularly clearly in the channel maps between $-52$ and $-62$ km s$^{-1}$), with the velocity becoming more positive as we move northward along the filaments toward the Radio Arc. Such a velocity gradient is seen in the CS observations (SG87) and, remarkably, also in the ionized gas distribution (YZ86). Thus, we conclude that the H I gas is closely associated with the molecular and ionized materials.

Given the above conclusion, it is instructive to make a more detailed comparison of the distributions of dense molecular gas as traced by CS, and neutral hydrogen, across the Arches. In doing so one must obviously be aware of the fact that the H I absorption data is limited to gas lying in front of continuum emission, while the CS data traces dense gas throughout the whole region.

Figure 11 shows the map of CS $J = 2 \rightarrow 1$ emission (SG87) integrated between 5 and $-55$ km s$^{-1}$ overlaid onto a gray scale of $\tau$(H I) integrated over five velocity channels giving an approximate range of $-15$ to $-65$ km s$^{-1}$. The $\tau$(H I) map has $\tau_{\mathrm{min}} = 0$ km s$^{-1}$ and $\tau_{\mathrm{max}} = 4.05$ km s$^{-1}$ and is plotted on a linear scale. Peaks 1 and 2 in the CS distribution (as referred to by SG87) are marked on the map, and a further, weaker peak, peak 3, is also marked. The range $-15$ to $-65$ km s$^{-1}$ in H I is chosen to best represent the negative velocity material associated with the Arches. In H I we are not able to include the gas from 5 to $-15$ km s$^{-1}$ since this is too heavily contaminated

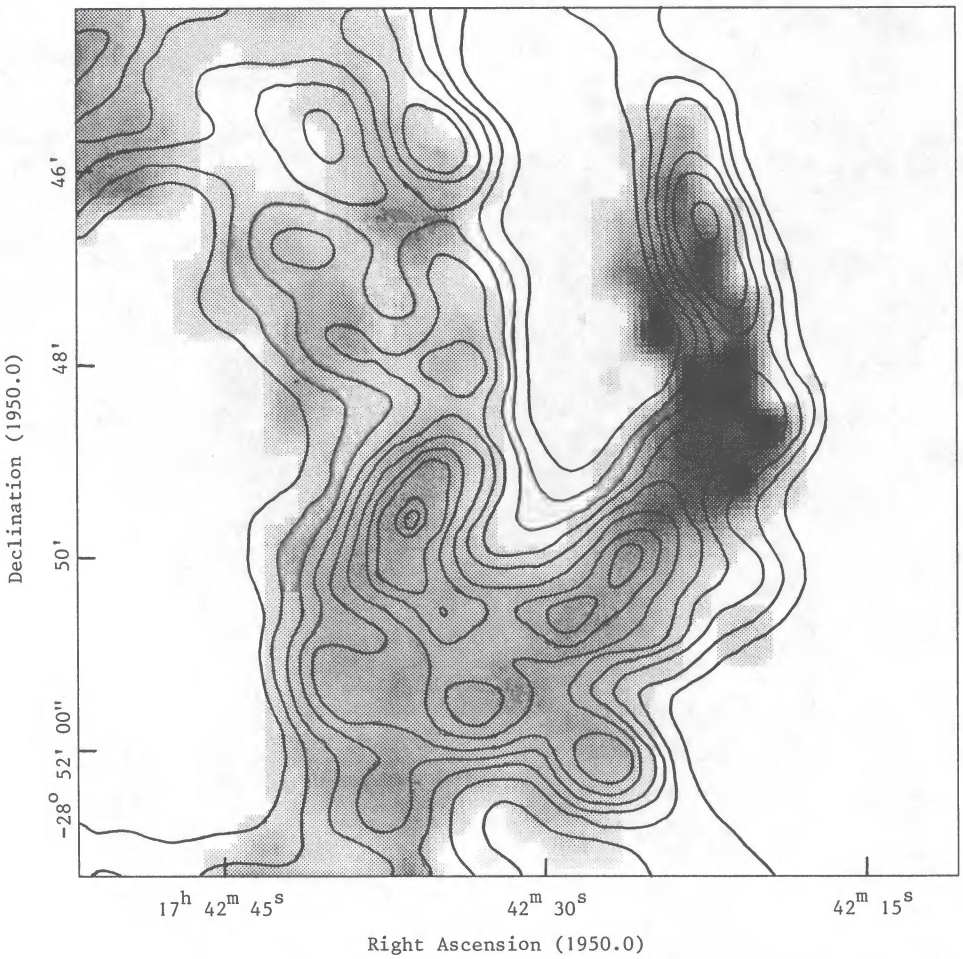


FIG. 12.—Gray-scale map of H I optical depth integrated over a 50 km $s^{-1}$ velocity interval between $-15$ and $-65$ km $s^{-1}$, overlaid onto the 20 cm contour map of the arched filaments taken from Fig. 1*b*. Continuum contour levels are 0.2, 0.3, 0.4, 0.51, 0.6, 0.75, 0.9, 1.0, 1.2, and 1.25 Jy $beam^{-1}$.

with line-of-sight material; a problem which does not occur with the denser CS gas.

Figure 12 shows a gray scale of H I optical depth (from about $-15$ to $-65$ km $s^{-1}$) over the arches region overlayed onto contours of the 20 cm radio continuum shown previously in Figure 1*b*. It is clear that, overall, the H I distribution does not closely follow the continuum distribution—indeed, over the westernmost filament there appears to be an anti-correlation between the peaks of $\tau$(H I) and the peaks of the radio continuum. This is most pronounced in the region $\alpha \simeq 17^h42^m23^s$, $\delta \simeq -28°49'30''$; here one sees a "gap" in the radio continuum where the emission is weaker than that observed from the rest of the filament. This gap coincides with a bar of intense H I optical depth and also with peak number 3 in the CS map. The implication is therefore that the apparent "gap" in the westernmost filament at this point is caused by absorbing material in front of, and probably associated with, the Arches.

Figure 7 of SG87 shows contours of CS emission (5 to $-55$ km $s^{-1}$) overlaid onto a 20 cm continuum radiograph of Sgr A and the Arc, and SG87 pointed out that there are a number of features in which the ionized structure lies along the edges of the molecular material, but that there are also a few regions where this trend is not followed, one example being peak 2. They suggest that such cases may be attributable to the ionization of line of sight cloud surfaces. We see from Figure 11 that there is some evidence of slightly enhanced H I optical depth around peak 2 but the H I, unlike the CS, shows no prominent

TABLE 1

$H_2$ COLUMN DENSITIES[a]

| Peak (1) | CS 2 → 1 (5, $-55$) km $s^{-1}$ (2) | $\tau$(HI) ($-15$, $-65$) km $s^{-1}$ (3) | Column (2) × 6/5 (4) |
|---|---|---|---|
| 1......... | $(26 \pm 13) \times 10^{22}$ | $\lesssim 3.5 \times 10^{22}$ | $\lesssim 4.2 \times 10^{22}$ |
| 2......... | $(17 \pm 8) \times 10^{22}$ | $\lesssim 3.5 \times 10^{22}$ | $\lesssim 4.2 \times 10^{22}$ |
| 3......... | $\sim 8.2 \times 10^{22}$ [b] | $\lesssim 7.3 \times 10^{22}$ | $\lesssim 8.8 \times 10^{22}$ |

[a] In centimeters$^{-2}$.

[b] Estimated from map.

1989ApJ...343..177L



peak there. The CS peak 1 does seem to have its outer edges ionized and occurs in a region where the radio continuum is weak or absent. As such, we do not expect the H I to show a peak (since our measurements are in absorption), and Figure 11 shows that there is no obvious H I enhancement at peak 1. We can estimate $H_2$ column densities from the H I optical depth map using equation (12) to give

$$N_{\rm col}(H_2)({\rm cm}^{-2}) \simeq \frac{\tau_v \Delta v({\rm km\ s^{-1}}) T_{\rm spin} \times 10^{21}}{5.49} . \quad (16)$$

(Here we have again assumed that $\beta \simeq 0.01$). Taking $T_{\rm spin} \lesssim 100$ K, will give upper limits on $N(H_2)$ over the approximate range $-15$ to $-65$ km s$^{-1}$, an interval of 50 km s$^{-1}$. To compare this with the SG87 estimates which are over the velocity interval $+5$ to $-55$ km s$^{-1}$ (an interval of 60 km s$^{-1}$), we can multiply by 6/5 for a crude comparison. Table 1 lists $N(H_2)$ column densities at peaks 1, 2, and 3 from SG87 and from this work.

Despite the considerable uncertainties involved in the estimation of $N(H_2)$ from both the CS and the H I data, it appears that over peaks 1 and 2 the column densities calculated from the H I observations are roughly a factor of 6 or so lower than those calculated from the CS data. However, the $N(H_2)$ values over peak 3 are in much better agreement. One might therefore be led to believe that around peaks 1 and 2 much of the CS molecular gas lies behind the ionized filaments and is therefore not accounted for in the calculations made using the H I optical depth maps. If true, this conclusion would indicate that peak 2 lies behind the ionized filaments (SG87 suggest that it may be an ionized cloud surface along the line of sight). The better agreement in the $H_2$ column densities over peak 3 suggest that the gas we are seeing here lies mostly in front of the filaments—and this is in good agreement with the previous suggestion that it is absorption by this material that causes the apparent "gap" in the ionized filaments.

Another aspect of the H I absorption seen at about $-30$ km s$^{-1}$ is the appearance of the sickle feature, G0.18$-$0.04, and sections of the Arc filaments. Figure 13 shows contours of 6 cm radio emission (YZ86) across the central Arc and sickle feature, overlaid onto a gray scale of H I optical depth in the channel centered on $-30$ km s$^{-1}$. There does appear to be tentative evidence for an anticorrelation of the H I gas with the radio continuum, particularly to the immediate north of the sickle: it

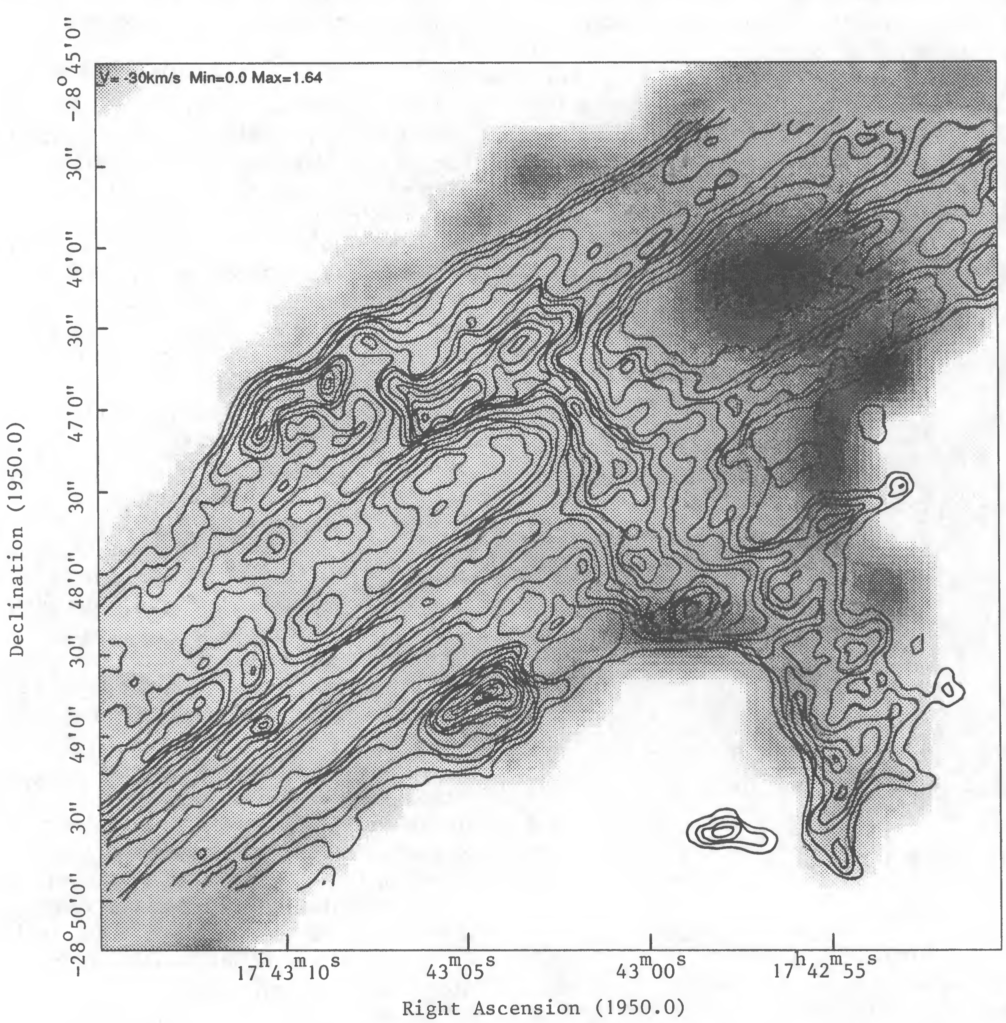


FIG. 13.—Contour map of 6 cm radio continuum emission over the region of the central Arc and sickle feature (Yusef-Zadeh 1986) superposed onto a gray scale of H I optical depth in the channel centered on $\sim -30$ km s$^{-1}$. The gray scale is linear and ranges from 0 to 1.64 km s$^{-1}$. 6 cm intensity contours are 2.5, 5, 7.5, 10, 15, 20, 25, ..., 65 mJy beam$^{-1}$.

is noted here that earlier recombination and molecular line studies of the Arc have shown no association or interaction between G0.18−0.04 and the negative velocity molecular gas. If the negative velocity material that we are seeing across G0.18−0.04 is part of the same body of gas seen over the Arches, the H I data suggest that it might be plausible to invoke a geometry in which the Arches and the −30 km s$^{-1}$ material are associated with each other and also with the Radio Arc, thus adding more weight to the arguments for the Arc and Arches being parts of a single, connected structure. However, while the $^{13}$CO and CS maps of Bally *et al.* (1987) between −30 and −10 km s$^{-1}$ *do* show a molecular condensation at the position of G0.18−0.04, this cloud appears to be detached from the −30 km s$^{-1}$ cloud associated with the arched filaments. Thus, one would expect to detect H I at these negative velocities in the vicinity of the sickle, and only if the atomic gas formed a bridging envelope between the two molecular condensations would the argument for a connection between the Arc and Arches be meaningful.

### *d) Sgr A Environment and Circumnuclear Molecular Ring about Sgr A**

A large fraction of recent molecular work at the Galactic center has focused on the rotating gas and dust ring at $R \sim 3$ pc, which surrounds the nonthermal compact radio source Sgr A*. A detailed discussion of the molecular ring will appear in a subsequent paper which will also deal with the kinematics and structure of the Sgr A environment as traced by H I. Therefore, here we will simply note that despite the relatively coarse resolution (~40″) of the H I observations described in this work, the molecular ring was clearly visible in the data. This is shown in the declination-velocity diagram through the right ascension of Sgr A* shown in Figure 14. The signature of the rotating ring is seen around ±100 km s$^{-1}$, while the contours at −120 to −140 km s$^{-1}$ represent absorption by the "expanding molecular ring" feature at $R \sim 200$ pc, to be discussed in § IV*e*. The remarkably clear appearance of the circumnuclear ring structure is almost certainly due to the statistical technique employed in the construction of the optical depth maps.

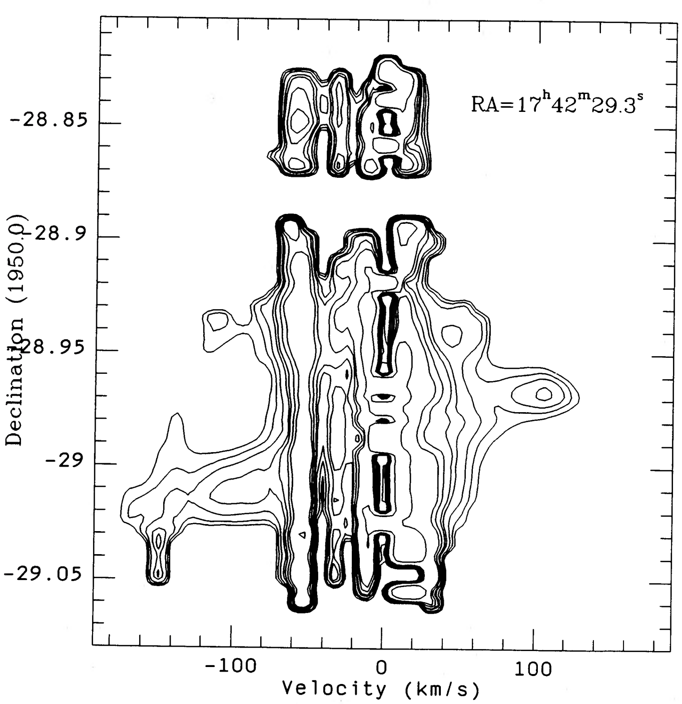


FIG. 14.—Declination-velocity map of H I optical depth ($\int_{\Delta v \simeq 10} \tau\, dv$) taken through the right ascension of Sgr A* (~17$^h$42$^m$29$^s$.3). Contour levels are 0.08, 0.1, 0.12, 0.17, 0.25, 0.5, and 1.0 km s$^{-1}$. The $R \sim 3$ pc circumnuclear molecular ring is clearly visible around ±100 km s$^{-1}$. The contours occurring around −120 to −140 km s$^{-1}$ represent absorption by the expanding ring feature at $R \sim 200$ pc as discussed in § IV*e*.

### *e) Expanding Molecular Ring Feature*

Figure 7*b* shows that there is a patch of absorption over the southern tip of the Arc occurring at about −130 to −140 km s$^{-1}$. This absorbing gas is from the feature thought to be the front section of an expanding molecular ring at $R \sim 200$ pc (see Bania 1977). The displacement of this material below the mean Galactic plane is consistent with the material at about −135 km s$^{-1}$ seen in $^{13}$CO and CS (Bally *et al.* 1987). Since we observe no absorption against the northern Arc by the rear section of this ring (~+170 km s$^{-1}$), it can thus be inferred that the Radio Arc does indeed lie within the ring, i.e., within ~200 pc of the Galactic center. This was also the conclusion reached by Güsten and Downes (1980) from their $H_2CO$ absorption observations of the region.

## V. CONCLUSIONS

The observations described in this paper provide useful information on the H I absorption within the inner ~80 pc of the Galaxy, thus extending the detailed knowledge available from previous high-resolution H I absorption synthesis studies of Sgr A. In addition, the angular scale of our H I observations make them directly comparable to recent molecular studies.

The results produced by applying the new statistical technique for making optical depth maps to the H I data have been very pleasing. Moreover, the method may be useful in a number of other situations where a resultant map is made from two or more initial maps and where the errors involved cause difficulties similar to those encountered in the H I data—such examples might be maps of spectral index and electron temperature.

Two of the most interesting outcomes of the absorption study were the absence of absorption across the Arc at +40 to 50 km s$^{-1}$, and the appearance at about +20 km s$^{-1}$ of absorption by material which could be depolarizing much of the synchrotron emission from the Arc filaments. Mapping this +20 km s$^{-1}$ material in CO (particularly $^{13}$CO) at high resolution may help to confirm or refute this suggestion.

An analysis of the negative velocity H I gas across the arched filaments showed a velocity gradient going from about −60 to about −10 km s$^{-1}$ moving northward along the filaments. This is in good agreement with the velocity structure as determined from recombination and molecular line data and thus strongly suggests an association between the H I gas and the ionized material. Estimates of $H_2$ column densities at various points in the Arches region have been compared with those estimates derived from molecular data. The results indicate that over some regions much of the molecular gas must lie behind the filaments but do not rule out any close association of molecular gas and filaments.

The clear appearance in the data of the circumnuclear ring about Sgr A* meant that model-fitting and rough density estimates were possible; the results of such a study will be presented elsewhere.

The large amount of useful data obtained from the H I study at this intermediate resolution suggests that it might also be profitable to carry out an OH-absorption study across the same region at similar resolutions.

We are grateful for the support provided by the VLA staff both during and after the observations. Particular thanks go to Alan Pedlar for his help and guidance in the initial production of large numbers of channel maps. We also express our appreciation to the referee for some useful comments on the paper.

## APPENDIX

## ESTIMATING ERRORS IN OPTICAL DEPTH MAPS

The problems of estimating errors in the derived values of the optical depth, $\tau$, were discussed briefly in the text. Here we address these problems via a Bayesian approach, in which we seek the conditional probability density function (p.d.f.) of $\tau_{\rm true}$ given the observations, i.e., $P(\tau_{\rm true} \mid \text{obsns})$. For further discussion of Bayesian methods see Jaynes (1983).

Bayes's Theorem is a particular application of the following law of conditional probabilities

$$P(A \mid B) = \frac{P(B \mid A)\, P(A)}{P(B)} \tag{1}$$

in which typically $A$ is the event that a given parameter has a certain value (which for our case is assumed to be continuously distributed) and $B$ is the event that the data has the value observed. If we are interested in the left-hand side of equation (1) as a function of $A$ only, we then have

$$P(A \mid B) \propto P(B \mid A)\, P(A)\,. \tag{2}$$

If there is no prior information which might bias our beliefs about $A$, it is reasonable to model it by a uniform "prior distribution," i.e., $P(A) = constant$ for all admissible $A$. In applying the Bayesian analysis to the $\tau$ data, we will choose to assume constant priors—the ultimate justification for this choice is that the inversion produces sensible results.

If $x$ and $y$ are the observed values of $I_l - I_c$ and $I_c$, and we assume that $x$ and $y$ are normally distributed about their true values $\mu_x$ and $\mu_y$ with variances $\sigma_x{}^2$ and $\sigma_y{}^2$, and also that their errors are independently distributed, then we can write the conditional probability of $x$ and $y$ given $\mu_x$ and $\mu_y$ as

$$P(x, y \mid \mu_x, \mu_y) = \frac{1}{2\pi\sigma_x \sigma_y} \exp\left\{-\frac{1}{2}\left[\frac{(x-\mu_x)^2}{\sigma_x{}^2} + \frac{(y-\mu_y)^2}{\sigma_y{}^2}\right]\right\}. \tag{3}$$

It is the $I_l$ noise that dominates in the $I_l - I_c$ maps, and since we *can* assume that the errors in $I_l$ and $I_c$ maps are independent, the same will therefore be approximately true for $I_l - I_c$ and $I_c$. Moreover, although the $I_l - I_c$ and $I_c$ maps will have correlated errors *before* the CLEANing process, it seems likely that these errors do indeed become decoupled after the CLEANing.

For some particular values of $x$ and $y$ it is therefore possible to calculate $\tau_{\rm obs}$, derive $P(\mu_x, \mu_y \mid x, y)$ and then construct $P(\tau_{\rm true} \mid x, y)$. From such a distribution it would be possible to determine whether there is, say, greater than 95% probability that the fractional error in $\tau_{\rm obs}$ is less than 20%. Points on the resultant map could thus be retained or rejected on this basis. In order to establish $P(\tau_{\rm true} \mid x, y)$ a numerical inversion of the p.d.f. $P(\tau_{\rm obs} \mid \mu_x, \mu_y)$ (itself generated by Monte Carlo simulations) was employed. The procedure is described below in five stages.

*Stage* 1.—We know that

$$\tau_{\rm true} = -\ln\left(1 + \frac{\mu_x}{\mu_y}\right), \tag{4}$$

and we therefore set

$$\tau_{\rm obs} = \begin{cases} \left(1 + \dfrac{x}{y}\right), & \text{if } x \le 0,\ y \ge 0 \quad \text{and} \quad |x| < y\,; \\ 0 & \text{otherwise}\,. \end{cases} \tag{5}$$

$P(\tau_{\rm obs} \mid \mu_x, \mu_y)$ is found from a Monte Carlo simulation in which random Gaussian noise is generated. We assume $\sigma_x$ and $\sigma_y$ are known from the individual maps, so that $x$ and $y$ are therefore taken from the normal distributions $N(\mu_x, \sigma_x)$ and $N(\mu_y, \sigma_y)$, respectively. At each iteration, $\tau_{\rm obs}$ is calculated from the $x$ and $y$ values generated and any inadmissible values are set to zero as in equation (5). A p.d.f. of $P(\tau_{\rm obs} \mid \mu_x, \mu_y)$ is thus built up over many iterations, and Figure 15 shows this p.d.f. in histogram form for various values of $\mu_x$ and $\mu_y$. Each histogram contains data from 2000 iterations, has 100 bins, and uses rms errors of $\sigma_x \sim 7$ mJy beam$^{-1}$ and $\sigma_y \sim 3$ mJy beam$^{-1}$, chosen so as to simulate the noise on the real data. When $\mu_x$ and $\mu_y$ differ significantly *and* $\tau_{\rm true}$ is small, the calculated distribution of $P(\tau_{\rm obs} \mid \mu_x, \mu_y)$ tends to peak about $\tau_{\rm true}$ and has an approximately Gaussian shape. However, when $\tau$ begins to increase and $|\mu_x|$ and $\mu_y$ become small and close in value, the distribution will show considerable spread with the peak moving away from $\tau_{\rm true}$—this behavior is illustrated well in Figure 15.

*Stage* 2.—The next stage is to generate p.d.f.'s $P(\tau_{\rm obs} \mid \mu_x, \mu_y)$ for a grid of values in $(\mu_x, \mu_y)$ space. Since $\tau_{\rm true} = -\ln(1 + \mu_x/\mu_y)$ and hence $\mu_y = \mu_x[\exp(-\tau) - 1]^{-1}$, there is a 1-1 mapping between $\mu_y$ and $\tau_{\rm true}$ for a given $\mu_x$, which therefore implies a 1-1 mapping between $(\mu_x, \mu_y)$ space and $(\tau_{\rm true}, \mu_x)$ space. As $\tau_{\rm true}$ is the parameter whose "distribution" we are seeking, it is then more sensible to work in $(\tau_{\rm true}, \mu_x)$ space. Thus, via the simulations we can produce values of $P(\tau_{\rm obs} \mid \tau_{\rm true}, \mu_x)$ over $(\tau_{\rm true}, \mu_x)$ space.

*Stage 3.*—The distribution we are seeking, $P(\tau_{\rm true} \mid \tau_{\rm obs}, \mu_x)$, can be estimated via a Bayesian inversion. Equation (6) gives an adaptation of the version of Bayes's Theorem given in equation (1):

$$P(A \mid B, C) = \frac{P(A \mid C)\, P(B \mid A, C)}{P(B \mid C)} \tag{6}$$

$$\Rightarrow P(\tau_{\rm true} \mid \tau_{\rm obs}, \mu_x) = \frac{P(\tau_{\rm obs} \mid \tau_{\rm true}, \mu_x)\, P(\tau_{\rm true} \mid \mu_x)}{P(\tau_{\rm obs} \mid \mu_x)} . \tag{7}$$

Now $\tau$ depends on the *ratio* $\mu_x : \mu_y$, thus, if we know $\mu_x$, $\tau$ is indeterminate unless $\mu_y$ is also known. Since we have no prior prejudices about $\mu_y$, it is sensible to take the distribution for $\tau_{\rm true}$ given $\mu_x$ alone as uniform, and in this case we then have

$$P(\tau_{\rm true} \mid \tau_{\rm obs}, \mu_x) \propto P(\tau_{\rm obs} \mid \tau_{\rm true}, \mu_x) . \tag{8}$$

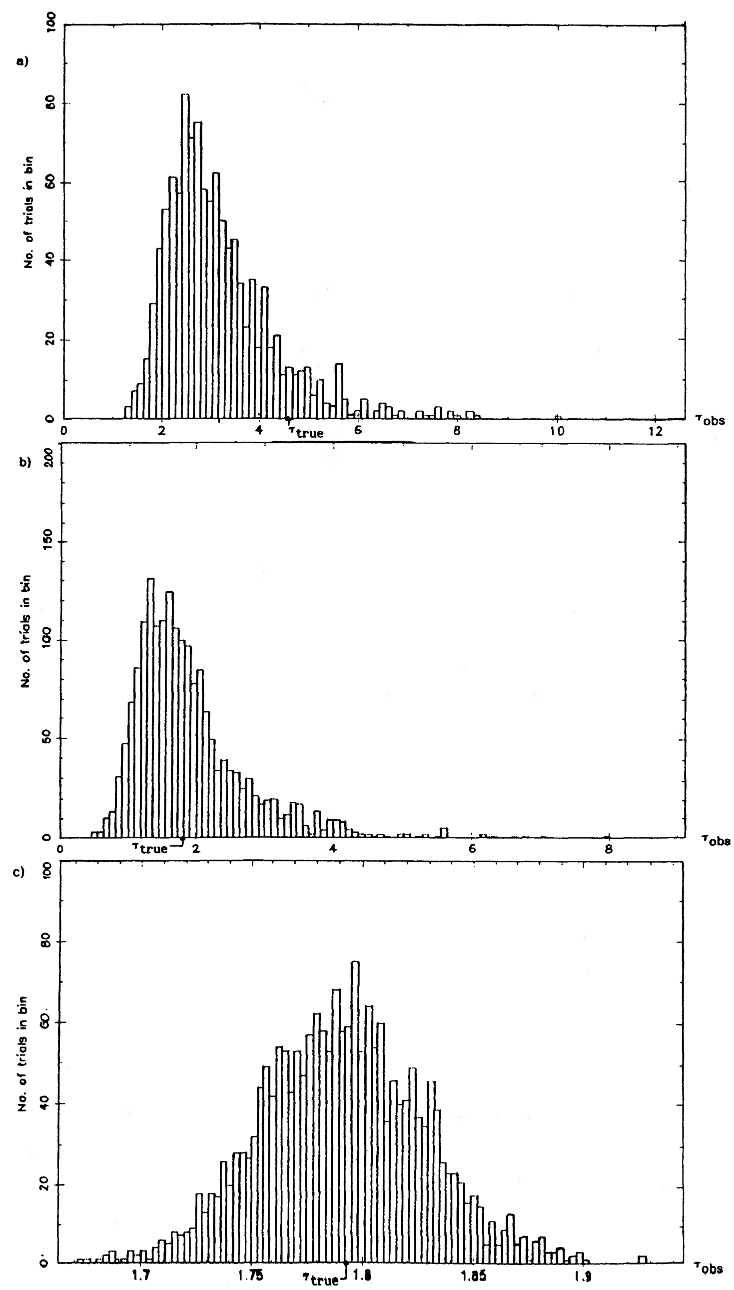


FIG. 15.—Histogram plots of $P(\tau_{\rm obs} \mid \mu_x, \mu_y)$ for (*a*) $\mu_x = -0.100$ Jy beam$^{-1}$, $\mu_y = 0.101$ Jy beam$^{-1}$ ($\tau_{\rm true} = 4.62$). (*b*) $\mu_x = -0.050$ Jy beam$^{-1}$, $\mu_y = 0.060$ Jy beam$^{-1}$ ($\tau_{\rm true} = 1.79$). (*c*) $\mu_x = -1.000$ Jy beam$^{-1}$, $\mu_y = 1.200$ Jy beam$^{-1}$ ($\tau_{\rm true} = 1.79$). Each plot was compiled from 2000 iterations and sorted into 100 bins, with $\sigma_x = 7$ mJy beam$^{-1}$ and $\sigma_y = 3$ mJy beam$^{-1}$ in each case.

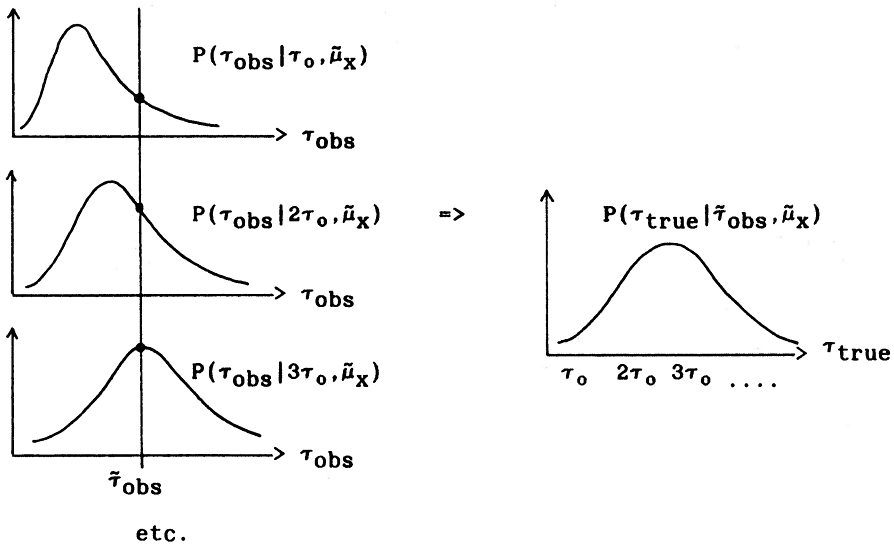


FIG. 16.—Illustration of how $P(\tau_{\rm true}\,|\,\tilde{\tau}_{\rm obs}, \tilde{\mu}_x)$, for given $\tilde{\tau}_{\rm obs}, \tilde{\mu}_x$, is built up from the distributions $P(\tau_{\rm obs}\,|\,n\tau_0, \tilde{\mu}_x)$, $n = 1, 2, 3, \ldots$

If $P(\tau_{\rm obs}\,|\,\tau_{\rm true}, \mu_x)$ is evaluated for a given $\mu_x = \tilde{\mu}_x$ and a *series* of values of $\tau_{\rm true}$, then $P(\tau_{\rm true}\,|\,\tilde{\tau}_{\rm obs}, \tilde{\mu}_x)$ can then be formed from this series of p.d.f.'s, as illustrated in Figure 16 ($\tilde{\tau}_{\rm obs}$ is some chosen value of $\tau_{\rm obs}$). In this way the $P(\tau_{\rm true}\,|\,\tau_{\rm obs}, \mu_x)$ distribution can be calculated for a grid of values in the $(\tau_{\rm obs}, \mu_x)$ plane.

*Stage 4.*—For given $\tau_{\rm obs}$ and $\mu_x$, say $\tilde{\tau}_{\rm obs}$ and $\tilde{\mu}_x$, we now calculate the 95% confidence interval for the p.d.f. $P(\tau_{\rm true}\,|\,\tilde{\tau}_{\rm obs}, \tilde{\mu}_x)$; i.e., we seek values $\tau_1$ and $\tau_2$ such that for $\tau_1 \leq \tau_{\rm true} \leq \tau_2$, $P(\tau_{\rm true}\,|\,\tilde{\tau}_{\rm obs}, \tilde{\mu}_x) > k_{95}$ and

$$\int_{\tau_1}^{\tau_2} P(\tau_{\rm true}\,|\,\tilde{\tau}_{\rm obs}, \tilde{\mu}_x)d\tau_{\rm true} = 0.95\ , \tag{9}$$

where $k_{95}$ is the value of the p.d.f. at both $\tau_1$ and $\tau_2$. In order to specify the Bayesian confidence interval we need to construct the interval so as to encompass a given area under the curve (the "confidence"), and in addition one must also give a criterion for the end points. Here we choose what seems the most natural criterion, namely, equal probability at both ends. The integration and estimation of confidence intervals are carried out numerically. The result is then that, for $\tau_{\rm obs} = \tilde{\tau}_{\rm obs}$ and $\mu_x = \tilde{\mu}_x$, the maximum fractional error, $\epsilon_{\rm max}$, is

$$\epsilon_{\rm max} = \frac{1}{\tilde{\tau}_{\rm obs}}\, {\rm Max}\, (|\,\tau_2 - \tilde{\tau}_{\rm obs}\,|, |\,\tilde{\tau}_{\rm obs} - \tau_1\,|)\ . \tag{10}$$

Thus, for these values of $\tau_{\rm obs}$ and $\mu_x$ we are $\sim$95% confident that the fractional error in $\tau_{\rm obs}$ is $\leq \epsilon_{\rm max} \times 100\%$.

*Stage 5.*—For a given $\mu_x$, $\tau_{\rm obs}$ is varied and $\epsilon_{\rm max}$ calculated until $\epsilon_{\rm max} \times 100 \simeq 20\%$; $\tau_{\rm crit}(20\%, \mu_x)$ is therefore defined as

$$\tau_{\rm obs} = \tau_{\rm crit}(20\%, \mu_x) \Leftrightarrow \epsilon_{\rm max} \times 100 = 20\%\ . \tag{11}$$

The above procedure is repeated to calculate $\tau_{\rm crit}$ for a number of $\mu_x$ values. Thus, given any $\mu_x$, only if $\tau_{\rm obs} \lesssim \tau_{\rm crit}(20\%, \mu_x)$ can we be $\sim$95% confident that the errors in $\tau_{\rm obs}$ are less than 20%.

However, the observed quantities are $\tau_{\rm obs}$ and $x$, *not* $\tau_{\rm obs}$ and $\mu_x$. In order to apply the above criterion to the map-making process we must therefore be sure that, in the graph of $\tau_{\rm crit}$ versus $\mu_x$, small changes of the order of the noise will produce correspondingly small changes in $\tau_{\rm crit}$.

Figure 17 shows a plot of $\tau_{\rm crit}$ versus $|\,\mu_x\,|$ using $\sigma_x = 7$ mJy beam$^{-1}$ and $\sigma_y = 3$ mJy beam$^{-1}$. To obtain a functional form for $\tau_{\rm crit} = f(\mu_x)$ one can then make a polynomial fit to this graph.

For $|\,\mu_x\,| \geq 0.15$ small changes in $|\,\mu_x\,|$ of the order of the noise produce very small changes in $\tau_{\rm crit}$, and therefore over this region we can justifiably take $x \cong \mu_x$. However, for $0.10 < |\,\mu_x\,| < 0.15$ variations of the order of the noise in $|\,\mu_x\,|$ *can* produce sizable errors in $\tau_{\rm crit}$. Over this region a criterion $\tau_{\rm obs} < \tau_{\rm crit} + \lambda$ is applied, where $\lambda$ is determined from the graph. A cutoff is imposed for $|\,\mu_x\,| < 0.1$ since it is unclear how $\tau_{\rm crit}$ behaves here. An additional cutoff for $y < 0.05$ is included since all believable structures in the continuum map have values above this figure.

Thus, given two maps, and a point at which $x$ and $y$ are known, we create a third map of $\tau_{\rm obs}$ where

$$\tau_{\rm obs} = \begin{cases} 0 & \text{for } |\,x\,| < 0.1 \text{ and } y < 0.05\ , \\ -\ln(1 + x/y) & \text{if } \tau_{\rm obs} \leq \tau_{\rm crit}(20\%, x) \text{ (from graph), or } \leq \tau_{\rm crit} + \lambda \text{ for } 0.1 < |\,\mu_x\,| < 0.15\ , \\ 0 & \text{otherwise}\ . \end{cases} \tag{12}$$

Thus, any value of $\tau_{\rm obs}$ on the resultant map is accurate in the following sense: *We can be $\sim$95% confident that the fractional error $\tau_{\rm obs}$ is at most 20%, and in the majority of cases is much less.*

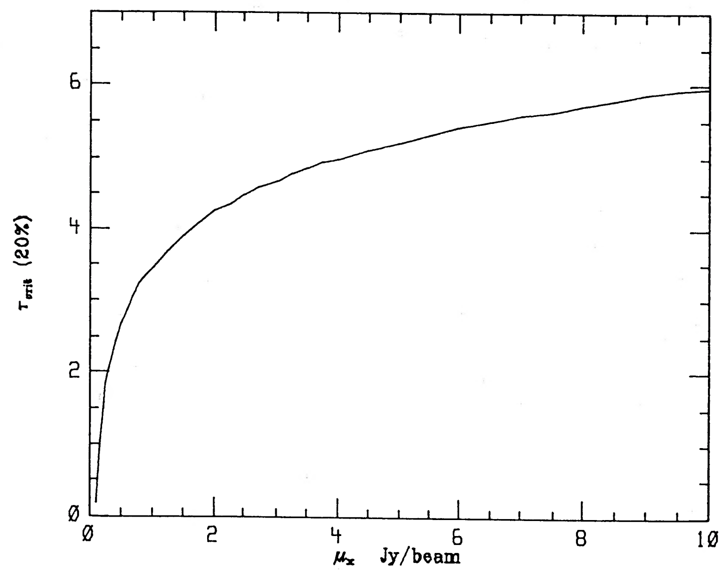


FIG. 17.—Curve of $|\mu_x|$ (Jy beam$^{-1}$) vs. $\tau_{crit}(20\%)$ for a model in which $\sigma_x = 7$ mJy beam$^{-1}$ and $\sigma_y = 3$ mJy beam$^{-1}$

## REFERENCES


Anantharamaiah, K., and Yusef-Zadeh, F. 1989, *IAU Symposium 136, The Galactic Center*, ed. M. Morris (Dordrecht: Reidel), in press.
Bally, J., Stark, A. A., Wilson, R. W., and Henkel, C. 1987, *Ap. J. Suppl.*, **65**, 13.
———. 1988, *Ap. J.*, **324**, 223.
Bania, T. M. 1977, *Ap. J.*, **216**, 381.
Brown, R. L., and Liszt, H. S. 1984, *Ann. Rev. Astr. Ap.*, **22**, 223.
Burn, B. J. 1966, *M.N.R.A.S.*, **133**, 67.
Clark, B. G. 1980, *Astr. Ap.*, **89**, 377.
Dent, W. A., Werner, M. W., Gatley, I., Becklin, E. E., Hildebrand, R. H., Keene, J., and Whitcomb, S. E. 1982, in *AIP Conf. Proc. No. 83, The Galactic Center*, ed. G. R. Riegler, R. D. Blandford (New York: AIP), p. 33.
Frerking, M. A., Langer, W. D., and Wilson, R. W. 1982, *Ap. J.*, **262**, 590.
Güsten, R., and Downes, D. 1980, *Astr. Ap.*, **87**, 6.
Güsten, R., Walmsley, C. M., and Pauls, T. 1981, *Astr. Ap.*, **103**, 197.
Inoue, M., Fomalont, E., Tsuboi, M., Yusef-Zadeh, F., Morris, M., Tabara, H., and Kato, T. 1989, *IAU Symposium 136, The Galactic Center*, ed. M. Morris (Dordrecht: Reidel), in press.
Inoue, M., Takahashi, T., Tabara, H., Kato, T., and Tsuboi, M. 1984, *Pub. Astr. Soc. Japan*, **36**, 633 (I84).
Jaynes, E. T. 1983, *Papers on Probability, Statistics, and Statistical Physics* (Collected Works), ed. R. D. Rosenkrantz (Dordrecht: Reidel).
Laing, R. 1984, in *Proc. NRAO Workshop No. 9, The Physics of Energy Transport in Extragalactic Radio Sources*, ed. A. Bridle and J. Eilek (Greenbank, WV: NRAO), p. 90.
Lasenby, J., Lasenby, A. N., and Yusef-Zadeh, F. 1989, in preparation.
Lewtas, J. 1987, Ph.D. thesis, University of Cambridge.
Liszt, H. S., Burton, W. B., and van der Hulst, J. M. 1985, *Astr. Ap.*, **142**, 237.
Liszt, H. S., van der Hulst, J. M., Burton, W. B., and Ondrechen, M. P. 1983, *Astr. Ap.*, **126**, 341.
Pauls, T., and Mezger, P. G. 1980, *Astr. Ap.*, **85**, 26.
Radhakrishnan, V., and Sarma, N. V. G. 1980, *Astr. Ap.*, **85**, 249.
Reich, W., Sofue, Y., Wielebinski, R., and Seiradakis, J. H. 1987, *NRO Report*, No. 141.
Schwarz, U. J., Shaver, P. A., and Ekers, R. D. 1977, *Astr. Ap.*, **54**, 863.
Seiradakis, J. H., Lasenby, A. N., Yusef-Zadeh, F., Wielebinski, R., and Klein, U. 1985*a*, *Nature*, **317**, 697.
———. 1985*b*, private communication.
Serabyn, E., and Güsten, R. 1987, *Astr. Ap.*, **184**, 133 (SG87).
Sofue, Y., Reich, W., Inoue, M., and Seiradakis, J. H. 1987, *Publ. Astr. Soc. Japan*, **39**, 95 (S87).
Yusef-Zadeh, F. 1986, Ph.D. thesis, Columbia University (YZ86).
Yusef-Zadeh, F., Morris, M., and Chance, D. 1984, *Nature*, **310**, 557.


A. N. LASENBY and J. LASENBY: Mullard Radio Astronomy Observatory, Cavendish Laboratories, Madingley Road, Cambridge CB3 0HE, England, UK

F. YUSEF-ZADEH: Laboratory for Astronomy and Solar Physics, NASA-Goddard Space Flight Center, Mail Code 684, Greenbelt, MD 20771